Optimizing a Formation-of-Arrays (FoA) Satellite Antenna System for Very High-Throughput Communications

GIACOMO BACCI, Senior Member, IEEE
University of Pisa, Pisa, Italy

RICCARDO DE GAUDENZI, Fellow, IEEE
European Space Agency, Noordwijk, The Netherlands

MARCO LUISE, Fellow, IEEE
University of Pisa, Pisa, Italy
CNIT/University of Florence, Firenze, Italy

ELENA SEBASTIANI
WISER srl , Livorno, Italy

PIERO ANGELETTI, Senior Member, IEEE
JOSÉ RAMÓN GONZÁLEZ
European Space Agency, Noordwijk, The Netherlands

Manuscript received 25 July 2023; revised 1 December 2023; accepted 28 January 2024. Date of publication 8 February 2024; date of current version 11 June 2024.

DOI. No. 10.1109/TAES.2024.3363674

Refereeing of this contribution was handled by V. Weerackody.

This work was supported in part by European Union under the Italian National Recovery and Resilience Plan (NRRP) of NextGenerationEU, partnership on "Telecommunications of the Future" through "RESTART" program under Grant PE00000001, and in part by the Italian Ministry of Education and Research (MUR) in the framework of the FoReLab project (Departments of Excellence).

Authors' addresses: Giacomo Bacci is with the Dipartimento Ingegneria dell'Informazione, University of Pisa, 56122 Pisa, Italy, E-mail: (giacomo.bacci@unipi.it); Riccardo De Gaudenzi, Piero Angeletti, and José Ramón González are with European Space Agency, 2200 AG Noordwijk, The Netherlands, E-mail: (rdegaude@gmail.com; piero.angeletti@esa.int; Jose.Ramon.Gonzalez@esa.int); Marco Luise is with the Dipartimento Ingegneria dell'Informazione, University of Pisa, 56122 Pisa, Italy, and also with the CNIT/University of Florence, 50139 Firenze, Italy, E-mail: (marco.luise@unipi.it); Elena Sebastiani is with WISER srl, 57123 Livorno, Italy, E-mail: (elena.sebastiani@wiser.it). *(Corresponding author: Giacomo Bacci.)*

Formation of arrays (FoA) distributed antenna technology has recently been proposed to provide 5G-like mobile satellites services in the context of the integration of nonterrestrial with terrestrial networks—the overall system goal being a sufficiently high throughput in terms of bit rate per unit area on the ground. This large distributed array configuration (resulting from the formation of many satellites each carrying its own small antenna) must be carefully engineered to provide the desired benefits. In this article, we tackle some fundamental issues related to FoA design, namely, *frequency selectivity*, *power generation*, and *optimal formation configuration*. Concerning frequency selectivity, we evaluate the intrinsic FoA frequency response assuming a wideband signal, and suggest how to mitigate possible impairments from a communication system perspective. Regarding power generation, we show how to decouple the functions of antenna and solar arrays to come to a power-efficient satellite configuration and design. Finally, in terms of formation optimization, we investigate a *formation thinning* approach with random placement of satellites on a grid, leading to a significant reduction of secondary beams in the emission of the FoA as well as fully satisfying the constraints placed by optimum power generation.

I. INTRODUCTION

As is known, the effort of integrating a nonterrestrial segment into current 5G (terrestrial) networks and forthcoming 6G networks is formidable [1]. An analysis performed in [2] concluded that a real integration of the two segments, in particular allowing end-users to utilize a smartphone, calls for the adoption of radically new technologies, such as the distributed very-large antenna for low Earth orbit (LEO) and geostationary Earth orbit (GEO) satellites introduced in [3]: A FoA. The satellite systems currently deployed to provide direct to hand-held communications (e.g., Iridium, Globalstar, Thuraya, and Inmarsat) require dedicated satellite user terminals (UTs) with a size larger than a smartphone's, and with an external antenna to support services similar to those offered by 2.5G terrestrial networks. An exception is represented by the Apple mobile satellite messaging service able to operate on the most recent i-Phones. AST mobile [4] is aiming to provide direct to hand-held 4G-like services using a LEO constellation operating around 900 MHz with very large deployable phased arrays. In the frame of third generation partnership project (3GPP) nonterrestrial network (NTN), 5G standardization effort is directed in adapting 5G terrestrial standards to support the satellite mode [5], with initial focus on low rate data and voice services for the reasons outlined in [2]. Although in terms of system sizing our main focus will be on provising 4G-like (i.e., 5G legacy) services from LEO and GEO orbits exploiting large arrays, we believe that the solutions proposed in this article can be scaled up to cover more aggressive data rates as supported by terrestrial 5G networks and future 6G networks. Our 4G service target is justified by the fact that providing 4G-like data rates to a conventional terrestrial hand-held terminal already represents a big technological challenge for the space segment, in particular for a GEO orbit. In terms of our current performance targets, the reader can refer to [3], whereby we size the space segment to provide data rates in the order of Mbps to a conventional low-antenna gain

hand-held UT having the characteristic specified by 3GPP 5G NTN documents (e.g., [6]).

Coming to the subject and contribution of this article, [3] already performed a system-wide analysis from a communication performance perspective (end-user available bit-rate as well as area spectral efficiency) and computed the benefits coming from the adoption of that technology, but it did *not* address three relevant issues in the design and optimization of the FoA structure, namely, 1) intrinsic frequency selectivity of the FoA emission; 2) issues related to power generation to feed each FoA satellite; and 3) optimum configuration of the satellite formation to optimize radio emission and meet certain constraints related to power generation. The three topics that we have just mentioned are the ones that this article specifically addresses, performing a detailed analysis and providing for each a viable solution as follows.

1) Frequency selectivity is a well-known issue of antenna arrays [7], and it is particularly relevant when (very) large arrays are used with wideband modulated signals (or baseband signals altogether, as in audio/underwater signal processing). In the design of an FoA, one has to consider this issue both in the intrinsic behavior of the antenna array carried by each satellite, and in the formation alignment. Following the approach presented in [3], the FoA is intended to provide 5G-like services at S-band (carrier frequency $f_0 = 2.2\,\text{GHz}$) and with a signal bandwidth $B_{\text{RF}} = 60\,\text{MHz}$, so that the fractional bandwidth of the data-modulated signal is $B_{\text{RF}}/f_0 \simeq 3\%$: This setup cannot be considered narrowband for beamforming. Therefore, frequency selectivity may have a nonnegligible impact on the digital link performance, and it has to be analyzed in detail—the subject of Section III to follow.
2) Issues related to power generation arise if we assume that the array carried by each satellite has the double function of radiating radio signal from one face, as well as providing electrical power to the satellite by carrying solar cells on the other side [3]. This is the simplest arrangement for a small satellite, but it is strongly suboptimal (as we will see later on) for GEO power generation as the array has to necessarily point towards the Earth to sustain the communication link, and cannot track the Sun for optimum power generation. In addition, the tight formation envisaged in [3] may introduce inefficiencies in power generation: For certain Sun/Earth/FoA alignments, a solar array may block sunlight to another array of an adjacent satellite, thus diminishing power generation efficiency. To the best of the authors' knowledge, the problems described in this article, associated to the self-induced eclipses and the implications on the power subsystem sizing, are addressed for the first time. The main features of the power subsystem in LEO satellites with body-mounted solar arrays can be found in [8] and [9], and for GEO satellites, including a solar array drive mechanism (SADM), in [10] and [11]. We develop this issue in Section V, wherein we present a solution based on a more efficient design in which the functions of antenna and solar arrays are decoupled (in particular, the solar array is side-mounted), so that the two can be optimized separately considering the FoA geometry.
3) Adopting a side-mounted solar array places further constraints on the location of satellites into a formation, that have to be carefully considered to perform emission beam pattern optimization. We know that creating an FoA makes the antenna very large, therefore very narrowbeam, but the sparsity of the formation required to accommodate the solar generators (SGs) brings forth the undesired phenomenon of introducing secondary beams, akin to the *grating lobes* of a conventional periodic array [12]. The control of the sidelobes and grating lobes in a sparse array with subarray (SA) centres positioned on a regular grid requires a proper design of its geometry. We will show in the following that a simple probabilistic FoA design approach [13], [14], [15] can lead to good results. In particular, we will focus on the technique of *thinning* the formation of satellites out of a regular grid according to a certain probability law, so as to come to a desired number of satellites in the FoA and to mitigate the antenna sidelobes level near the wanted beam. In the thinning criterion, we also add a constraint on the satellites placement so as to keep the solar arrays of different satellites at a convenient distance—this approach is presented in Section IV, and extended in Section V to include the constraints placed by power generation. Finally, Section VI concludes this article.

For the reader's convenience, Table I reports the symbols and definitions that will be used throughout the article.

II. SYSTEM DESCRIPTION AND FEASIBILITY CONSIDERATIONS

A. System Aspects

The notion and general architecture of an FoA has been introduced in [3]. In the following, we will just recall a few key points to improve the understanding of the discussion in the following sections.

As shown in Fig. 1, the FoA is fed by a central satellite (CS) that connects the (many) network gateway(s) on ground to the different satellites of the FoA. Any up/down feeder link carries many individual beams' carriers multiplexed in frequency using a wideband radio frequency (RF) link. For the regional GEO scenario described in [3], the aggregate throughput can be in the order of hundreds of Gbps, hence a single RF link will not provide sufficient capacity even using Ka-band and high-order modulations. In this case, multiple gateways exploiting spatial diversity and full frequency reuse will be necessary, as is currently the case for any high throughput satellite (HTS) system.

TABLE I
Notation Used Throughout the Paper

parameter	*symbol*	*value/unit*
speed of light	c	m/s
frequency	f	Hz
carrier frequency	f_0	Hz
wavelength	λ	m
carrier wavelength	λ_0	m
baseband frequency	ν	Hz
signal bandwidth	B_{RF}	Hz
number of satellites in the FoA/TFoA	S	–
radiating element spacing within any SA	d	m
inter-satellite SA spacing (or grid spacing for TFoA)	Δ	m
satellite SA position error	$\boldsymbol{\delta}_s$	m
FoA array pattern elevation angle	θ	rad
FoA array pattern elevation angle at beam center	θ_0	rad
FoA array pattern azimuth angle	φ	rad
FoA array pattern azimuth angle at beam center	φ_0	rad
ancillary function #1	Ω	$\sin\theta$
ancillary function #2	Ψ	$\cos\theta\sin\varphi$
FoA global array response	ζ	–
FoA factor	ζ'	–
Single SA factor	ζ''	–
number of potential satellite locations (TFoA)	G_s	
number of radiating elements per satellite SA	N	–
probability of occupancy of a TFoA grid location	q_s	–
FoA grid location occupancy indicator	ξ_s	–
average number of TFoA satellites	$\overline{S}$	–
TFoA satellite density	δ	–
TFoA probability function	ρ_s	–
standard deviation of position error	σ	m

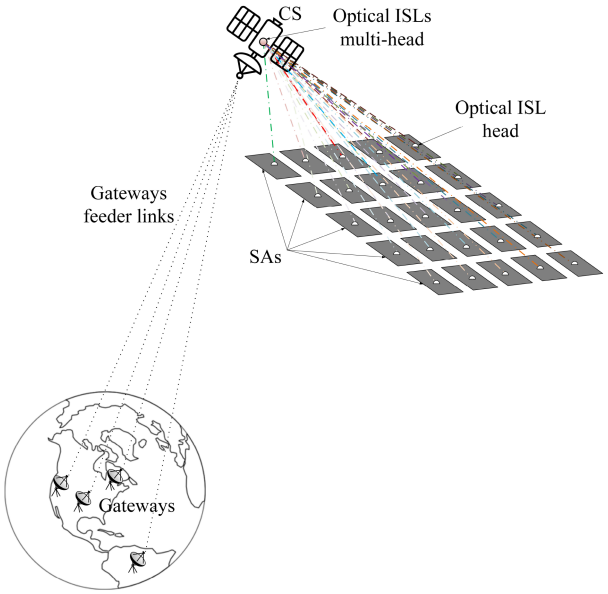

Fig. 1. Illustration of the FoA and of its ancillary components—CS: central satellite, SA: FoA satellite' subarray, ISL: intersatellite link.

All of the gateways' feeder links carriers received by the CS are down-converted to baseband and digitized, and the relevant I/Q baseband digital samples are routed to a high-throughput digital processor.

The processor implements digital beamforming for all of the FoA beams. In this respect, two different approaches for beamforming are possible, i.e., centralized at the CS, or decentralized at the level of each single FoA satellite, with the former approach best suited for the GEO case, while the latter is more suitable for LEO case for the reasons explained in [3, Section V]. Following again the approach sketched in [3], the digital signals corresponding to each individual radiating element of all FoA SAs are converted to an optical-modulated signal, and the different optical signals are wavelength-division multiplexed to create an aggregate optical digital carrier feeding the optical head pointed towards each FoA satellite (implementing a short-span optical intersatellite link (ISL)). Once received by the optical receiver on board the relevant FoA satellite, the optical digital stream is de-multiplexed, each component being converted back to digital I/Q and finally remodulated onto an analog S-band carrier to feed the diverse radiating elements of the SA.

The different SAs composing the satellite antenna are connected via an optical ISL to a so-called CS, which is providing the feeder link connection to the gateway station on ground. The CS also takes care of the crucial functions of: 1) calibration of the signal paths going to the individual satellites; and 2) control of the formation flying geometry. The interested reader can refer to [16], [17], [18], [19], [20], [21], [22], and [23] and related references for a review of the different techniques to keep satellites in formation flying.

Once the architectural issues above are clear, there is no further conceptual difference in terms of beam/traffic management between the (distributed) FoA and a (centralized) single-satellite system featuring phased array technology to implement a multibeam antenna pattern. For example, the simple heuristic, yet high-performance, resource allocation solutions devised for a phased-array based multibeam HTS network, reported in [24], [25], and [26], are also applicable to the FoA case. It is remarked that these solutions are not requiring to dynamically modify the single array element transmitted power to adapt to the typical nonuniform traffic distributions, thus simplifying the active antenna design and implementation.

B. Feasibility Considerations

The notion of an FoA is definitely challenging in technological terms, but its motivation can be given in a nutshell as follows. The analysis in [3] indicated that 4G-like communications services to a hand-held mobile terminal can be provided from a LEO orbit with an antenna of size $11 \times 11\,\mathrm{m}^2$, that is also technologically achievable with a mechanically deployable phased array. The same services can on the contrary be provided from GEO orbit (only) adopting an array size in excess of $120 \times 120\,\mathrm{m}^2$, that is only feasible resorting to the FoA approach. Clearly this array size cannot be easily achieved by means of a deployable array technology, and hence the interest for the FoA concept. We will show that, while for LEO satellites a body mounted SG can work, this is not the case for the GEO case, as the body generated eclipse will curtail the power generated on-board the satellites. The SA spacing required to counteract this issue is making the inorbit assembly for GEO even less attractive.

In our opinion, a GEO single-FoA solution is more desirable than a LEO constellation of satellites for a number of reasons. First, a LEO-based direct to hand-held service requires launching and maintaining hundreds to thousands of satellites, each equipped with a large deployable phased

array. The regional GEO (R-GEO) FoA approach will require launching a similar amount of smaller satellites with a smaller array size and a much longer lifetime. In addition, deploying a reasonably-operating LEO constellation requires launching a considerably high fraction of all of the envisaged satellites—on the contrary, the deployment of the GEO FoA satellites can be scalably graduated, starting from a initial lower number configuration, progressively matching the increasing market traffic request over the area of interest. Finally, RF spectrum for direct to hand-held mobile services is a very scarce resource, so that frequency reuse, whenever possible, is highly recommended and desired. Unfortunately, handheld mobile user equipments (UEs) do not provide any antenna spatial discrimination, therefore two different LEO global systems sharing the same frequency band cannot coexist, unless the two serve nonoverlapped areas, at the cost of throughput and/or coverage reduction. On the contrary, *regional* GEO systems are by design deployed to cover nonoverlapping regions, and can be tailored and optimized for a specific geographical area, with full frequency reuse across different coverage areas.

The objective of the analysis to follow, rather than making a cost-benefit analysis of the different solutions to address the direct to hand-held mobile services, is just to identify and derisk possible technical areas related to the implementation of very large active antennas, which represents a key technology for developing cost-attractive system solutions. The issues investigated in this article are also of interest in case one prefers to implement a distributed array either by means of mechanically deployable panels, or by hybrid use of a formation on satellites with mechanically deployable panels, or with advanced inorbit assembly solutions.

The other challenges that are being investigated by experts in other fields are related to the techniques for satellite formation flying tight control and swarm synchronization as well as how to support multiple optical intersatellite links as required by the CS.

In addition to the specific service considered in this article, there is a clear trend to increase the satellite array antenna size to improve end-user performance at an affordable cost. This trend is also occurring for higher frequency bands. The issue of how to counteract large antenna array(s) frequency selectivity and how to power a large GEO array with acceptable antenna pattern investigated in this contribution are therefore of high interest for other applications.

III. FREQUENCY SELECTIVITY OF THE FOA AND ITS CURE

A. Geometrical Analysis of the FoA

The issue of frequency selectivity of a large array of radiating elements is well known [7]. Frequency dispersion has a significant effect on the radiation pattern of phased arrays with implications for the array's performance, especially in broadband (relative to the central frequency) applications. Early contributions examined basic mechanisms degrading passive arrays performance as frequency is changed [27], [28].

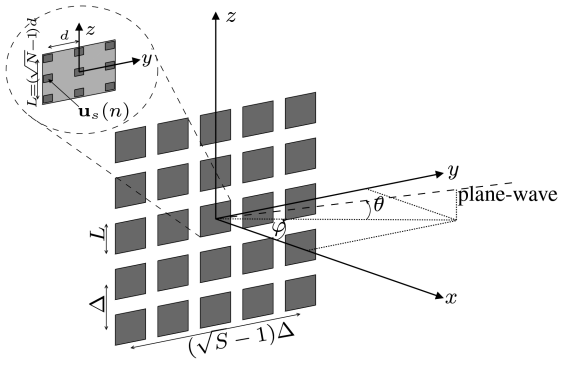

Fig. 2. FoA square-shaped configuration, with $S = 25$ satellites (arrays), located in the yz-plane, each hosting $N = 9$ radiating elements with spacing d, also showing a transmitted plane wave with elevation θ and azimuth φ.

Electronic-scanning RADARs have been the first systems making use of large phased arrays, and frequency dispersion effects on pulsed and chirped signals have been thoroughly analyzed and understood for these systems [29], [30], [31], [32]. Countermeasures to limit the detrimental effect of frequency dispersion have been also readily identified in substituting the phase control elements with true time delay elements [33], [34]. Considering the higher cost and complexity of delay elements with respect to phase shifters, hybrid architectures have been also proposed [7], [33].

Generally speaking, factors that contribute to the phased array performance include: The array geometry, the number of elements, the element spacing, the maximum scan angle, and the instantaneous bandwidth. As far as frequency selectivity is concerned, the wider the signal bandwidth B_{RF}, the larger the selectivity effect. In our FoA, the source of selectivity is actually the large size of the *formation* rather than that of the individual satellite antennas.

Let us analyze this effect starting back from the simple rectangular-grid FoA configuration analyzed in [3] and shown in Fig. 2, encompassing S satellites, each equipped with a simple active square array of N elements, whose combined formation/array factor turns out to be[1]

$$\zeta(\varphi,\theta)=\Big|\underbrace{\zeta'(\varphi,\theta)}_{\text{FoA factor}}\cdot\underbrace{\zeta''(\varphi,\theta)}_{\text{array factor}}\Big|^2, \tag{1}$$

where φ and θ denote the azimuth and elevation angles of a generic location in space, respectively, and

$$\zeta'(\varphi,\theta)=\frac{\sin\left[\pi\sqrt{S}\sin(\theta)\frac{\Delta}{\lambda}\right]\sin\left[\pi\sqrt{S}\cos(\theta)\sin(\varphi)\frac{\Delta}{\lambda}\right]}{\sin\left[\pi\sin(\theta)\frac{\Delta}{\lambda}\right]\sin\left[\pi\cos(\theta)\sin(\varphi)\frac{\Delta}{\lambda}\right]}, \tag{2}$$

[1] We do not include here the satellite array single-element radiation pattern as in [3], that is not essential to the discussion and can be included in a straightforward way.

$$\zeta''(\varphi,\theta)=\frac{\sin\left[\pi\sqrt{N}\sin(\theta)\frac{d}{\lambda}\right]\sin\left[\pi\sqrt{N}\cos(\theta)\sin(\varphi)\frac{d}{\lambda}\right]}{\sin\left[\pi\sin(\theta)\frac{d}{\lambda}\right]\sin\left[\pi\cos(\theta)\sin(\varphi)\frac{d}{\lambda}\right]}, \tag{3}$$

and where λ is the radio wavelength. The parameters d and Δ represent the spacing of the regular square grid of the array elements in each satellite antenna, and of the satellites in the formation, respectively. Introducing the oscillation frequency $f=c/\lambda$ (with c denoting the speed of light), we get the expression of the *frequency-dependent* array factor

$$\zeta(\varphi,\theta;f)=\left|\frac{\sin\left[\pi\sqrt{S}\Omega(\theta)\Delta\frac{f}{c}\right]\sin\left[\pi\sqrt{S}\Psi(\varphi,\theta)\Delta\frac{f}{c}\right]}{\sin\left[\pi\Omega(\theta)\Delta\frac{f}{c}\right]\sin\left[\pi\Psi(\varphi,\theta)\Delta\frac{f}{c}\right]}\right. \times\left.\frac{\sin\left[\pi\sqrt{N}\Omega(\theta)d\frac{f}{c}\right]\sin\left[\pi\sqrt{N}\Psi(\varphi,\theta)d\frac{f}{c}\right]}{\sin\left[\pi\Omega(\theta)d\frac{f}{c}\right]\sin\left[\pi\Psi(\varphi,\theta)d\frac{f}{c}\right]}\right|^2, \tag{4}$$

where for simplicity $\Omega(\theta)=\sin\theta$ and $\Psi(\varphi,\theta)=\cos\theta\sin\varphi$. We consider now a *wideband modulated signal* spanning a radio bandwidth B_{RF} around a carrier frequency $f_0=c/\lambda_0$. The generic frequency f of any spectral component of this signal can be cast for convenience into the form $f=f_0+\nu$, $\nu\in[-B_{\mathrm{RF}}/2,+B_{\mathrm{RF}}/2]$, where ν is in practice the *baseband frequency* spanning the bandwidth of the *baseband equivalent* (also known as the *complex envelope*) of the modulated signal. With this notation, the (baseband-frequency-dependent) array factor becomes

$$\begin{aligned}\zeta(\varphi,\theta;\nu)=&\left|\frac{\sin\left[\pi\sqrt{S}\Omega(\theta)\frac{\Delta}{\lambda_0}\left(1+\frac{\nu}{f_0}\right)\right]}{\sin\left[\pi\Omega(\theta)\frac{\Delta}{\lambda_0}\left(1+\frac{\nu}{f_0}\right)\right]}\right.\\ &\times\frac{\sin\left[\pi\sqrt{S}\Psi(\varphi,\theta)\frac{\Delta}{\lambda_0}\left(1+\frac{\nu}{f_0}\right)\right]}{\sin\left[\pi\Psi(\varphi,\theta)\frac{\Delta}{\lambda_0}\left(1+\frac{\nu}{f_0}\right)\right]}\\ &\times\frac{\sin\left[\pi\sqrt{N}\Omega(\theta)\frac{d}{\lambda_0}\left(1+\frac{\nu}{f_0}\right)\right]}{\sin\left[\pi\Omega(\theta)\frac{d}{\lambda_0}\left(1+\frac{\nu}{f_0}\right)\right]}\\ &\times\left.\frac{\sin\left[\pi\sqrt{N}\Psi(\varphi,\theta)\frac{d}{\lambda_0}\left(1+\frac{\nu}{f_0}\right)\right]}{\sin\left[\pi\Psi(\varphi,\theta)\frac{d}{\lambda_0}\left(1+\frac{\nu}{f_0}\right)\right]}\right|^2.\end{aligned} \tag{5}$$

Frequency selectivity is in general caused by the factor $(1+\nu/f_0)$, but it is actually relevant only if this factor is significantly different from 1 for $\nu\in[-B_{\mathrm{RF}}/2,+B_{\mathrm{RF}}/2]$, e.g., if the signal bandwidth B_{RF} is from 5% to 10% of the carrier frequency. The selectivity effect is in general *not* symmetric with respect to (wrt) to the carrier frequency as the function $\sin(\alpha_0+\Delta\alpha)$ is not symmetric wrt $\Delta\alpha$ for $\alpha_0\neq 0$.

Assuming that we are dealing with a wideband signal (in the sense mentioned above), the selectivity effect depends on the user location in terms of coordinates (φ,θ). From (5) we see that there is no frequency selectivity at all whenever $\varphi=\theta=0$, i.e., at the center of the nadir-pointing FoA beam. On the contrary, the effect is slightly "enhanced" when any of the factors $\sqrt{S}\Omega(\theta)$, $\sqrt{S}\Psi(\varphi,\theta)$, $\sqrt{N}\Omega(\theta)$, and $\sqrt{N}\Psi(\varphi,\theta)$ tend to increase, i.e., when we move towards the edge of the beam.

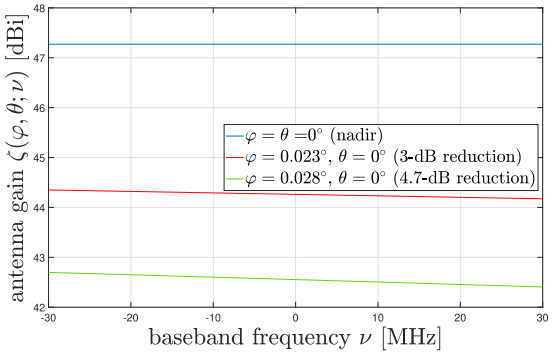

Fig. 3. Frequency selectivity of the FoA factor for a GEO configuration with $S=1089$ and $N=49$.

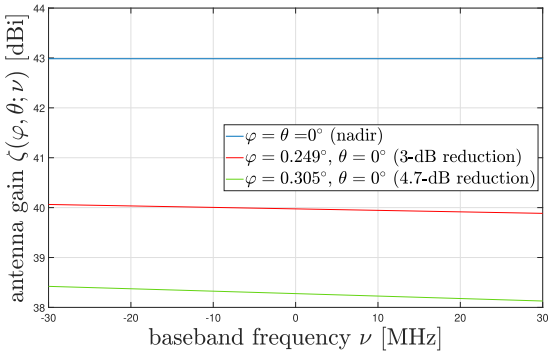

Fig. 4. Frequency selectivity of the FoA factor for a LEO configuration with $S=9$ and $N=2209$.

Fig. 3 shows the selectivity effect for the configuration envisaged in [3] for a GEO FoA with $S=1089$ and $N=49$, using $f_0=2.2\,\mathrm{GHz}$, $d=4.5\lambda_0\approx 61.3\,\mathrm{cm}$, $L=(\sqrt{N}-1)d\approx 3.68\,\mathrm{m}$, and $\Delta=1.25L\approx 4.6\,\mathrm{m}$. The blue line depicts the case $\varphi=\theta=0°$, whereas the red and the green curves report the results for $\varphi=0.023°$ (3-dB reduction) and $\varphi=0.028°$ (4.7-dB reduction),[2] respectively, both with $\theta=0°$. As expected, the selectivity effect, albeit actually present, is barely noticeable across the assumed 60-MHz bandwidth, and could be safely neglected—although we showed results on the azimuth plane only, the reader can verify that this conclusion basically holds for any direction (φ,θ).

The same behavior can be observed in Fig. 4, which reports the selectivity for a LEO-like configuration with $S=9$ and $N=2209$. In this case, $f_0=2.2\,\mathrm{GHz}$, $d=0.6\lambda_0\approx 8.2\,\mathrm{cm}$, $L=(\sqrt{N}-1)d\approx 3.76\,\mathrm{m}$, and $\Delta=1.25L\approx 4.7\,\mathrm{m}$ (see [3] for further details on this set of system parameters).

[2]The two values −3 and −4.7 dB represent conventional definitions of the beam edge on Earth in the case of aggressive (beams very close to each other) and less aggressive beam pattern design, respectively.

B. Narrowband Beam Steering

The system analysis performed in [3] envisaged the creation of a multibeam communication network with relatively narrow beams (comparable to the size of a terrestrial rural cell). Such a network was implemented through a strategy of beam steering (beamforming) applied to the FoA: Each beam was obtained by appropriately steering the main FoA beam towards a desired beam center (φ_0, θ_0) to serve a certain population of users on ground.

The conventional approach to array beam steering is applying a set of appropriate *phase shifts* (either at baseband or at RF) to the different radiating elements of the antenna array. In our FoA, we have the option to: *i*) implement beam steering at the formation level only, i.e., by applying the same phase shift to all of the elements of a single array, those shifts being different from satellite to satellite; or *ii*) applying different phase shift individually to all of the radiating elements of the satellite arrays. Whatever the option is (we will investigate the two options later on), the approach is anyway called *narrowband* steering, because it is devised for a theoretically monochromatic signal at the carrier frequency, and it is approximately valid (only) in the case the modulated signal is quasi-monochromatic, i.e., narrowband [7].

The FoA factor with narrowband steering in the most general case of radiating-element-level (i.e., formation and satellite) phase shift is found to be

$$\zeta_{\mathrm{NB}}(\varphi,\theta;\varphi_0,\theta_0;\nu) = \Big|\underbrace{\zeta'_{\mathrm{NB}}(\varphi,\theta;\varphi_0,\theta_0;\nu)}_{\text{FoA factor}}\cdot\underbrace{\zeta''_{\mathrm{NB}}(\varphi,\theta;\varphi_0,\theta_0;\nu)}_{\text{array factor}}\Big|^2, \quad (6)$$

where

$$\zeta'_{\mathrm{NB}}(\varphi,\theta;\varphi_0,\theta_0;\nu) = \frac{\sin\left\{\pi\sqrt{S}\frac{\Delta}{\lambda}\left[\Omega(\theta)\left(1+\frac{\nu}{f_0}\right)-\Omega(\theta_0)\right]\right\}}{\sin\left\{\pi\frac{\Delta}{\lambda}\left[\Omega(\theta)\left(1+\frac{\nu}{f_0}\right)-\Omega(\theta_0)\right]\right\}} \times \frac{\sin\left\{\pi\sqrt{S}\frac{\Delta}{\lambda}\left[\Psi(\varphi,\theta)\left(1+\frac{\nu}{f_0}\right)-\Psi(\varphi_0,\theta_0)\right]\right\}}{\sin\left\{\pi\frac{\Delta}{\lambda}\left[\Psi(\varphi,\theta)\left(1+\frac{\nu}{f_0}\right)-\Psi(\varphi_0,\theta_0)\right]\right\}}, \quad (7)$$

$$\zeta''_{\mathrm{NB}}(\varphi,\theta;\varphi_0,\theta_0;\nu) = \frac{\sin\left\{\pi\sqrt{N}\frac{d}{\lambda}\left[\Omega(\theta)\left(1+\frac{\nu}{f_0}\right)-\Omega(\theta_0)\right]\right\}}{\sin\left\{\pi\frac{d}{\lambda}\left[\Omega(\theta)\left(1+\frac{\nu}{f_0}\right)-\Omega(\theta_0)\right]\right\}} \times \frac{\sin\left\{\pi\sqrt{N}\frac{d}{\lambda}\left[\Psi(\varphi,\theta)\left(1+\frac{\nu}{f_0}\right)-\Psi(\varphi_0,\theta_0)\right]\right\}}{\sin\left\{\pi\frac{d}{\lambda}\left[\Psi(\varphi,\theta)\left(1+\frac{\nu}{f_0}\right)-\Psi(\varphi_0,\theta_0)\right]\right\}}. \quad (8)$$

From this expression we can see that, unlike the unsteered configuration (5), some degree of selectivity is now present even along the main direction, i.e., $\theta = \theta_0$, $\varphi = \varphi_0$. This issue is well known, especially in the domain of audio and ultrasound signal processing [35], and it is often regarded another way round: Considering $\nu = \nu^\star \neq 0$, we see that the maximum gain (i.e., the direction for which the numerator and the denominator of the factors in (6) are equal to 0) is not at $\theta = \theta_0$ and $\varphi = \varphi_0$, but at another, different direction, given by $\theta^\star = \sin^{-1}[\Omega(\theta_0)/(1+\nu^\star/f_0)]$ and $\varphi^\star = \sin^{-1}\{\Psi(\varphi_0,\theta_0)/[\cos\theta^\star(1+\nu^\star/f_0)]\}$. This is considered as a steering error for the signal component at the frequency $\nu^\star$ and the beam is said to be *squint* at that frequency.

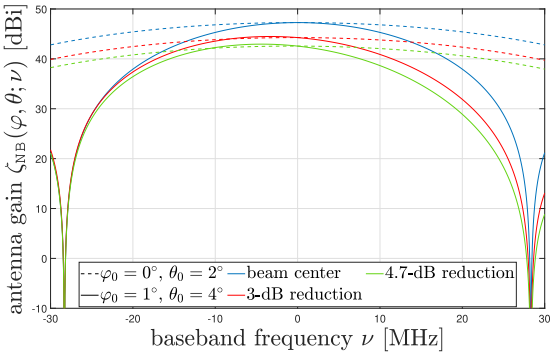

Fig. 5. Frequency selectivity of the FoA factor with narrowband steering for a GEO configuration with $S = 1089$ and $N = 49$: In the case $(\varphi_0 = 0°, \theta_0 = 2°)$, $\theta = \theta_0 = 2°$ in all curves, whilst $\varphi = \varphi_0 = 0°$, $\varphi = \varphi_0 = 0.023°$, and $\varphi = \varphi_0 = 0.028°$ for beam center, 3-dB reduction, and 4.7-dB reduction, respectively; In the case $(\varphi_0 = 1°, \theta_0 = 4°)$, $\theta = \theta_0 = 4°$, for all curves, whilst $\varphi = \varphi_0 = 1°$, $\varphi = \varphi_0 = 1.023°$, and $\varphi = \varphi_0 = 1.028°$, for beam center, 3-dB reduction, and 4.7-dB reduction, respectively.

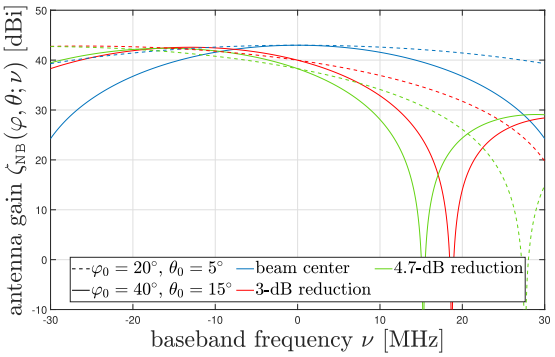

Fig. 6. Frequency selectivity of the FoA factor with narrowband steering for a LEO configuration with $S = 9$ and $N = 2209$.

Fig. 5 shows, using the same color code taken for Figs. 3 and 4, the dramatic effect of steering the beam on frequency selectivity for the GEO FoA configuration introduced in Section III-A and for two different beam centers: dashed lines refer to a the case $(\varphi_0 = 0°, \theta_0 = 2°)$, whereas solid lines depict $(\varphi_0 = 1°, \theta_0 = 4°)$. The mild behavior, observed in Fig. 3, is turned into a strong selectivity as long as we depart from the nadir direction, and has to be properly addressed not to incur in severe performance degradation of the satellite link on the most steered beams. Similar conclusions can be drawn for the LEO FoA configuration, using the results reported in Fig. 6.

The standard solution to a problem of frequency selectivity in terms of communication technologies is the adoption of orthogonal frequency division multiplexing (OFDM), with a subcarrier spacing so small that each subcarrier "sees" a substantially flat portion of the array frequency response [36]. It is true that this approach prevents distortion of the wideband received signal, but it does not prevent the subcarriers affected by a (very) low array response from being received with a (very) bad signal-to-noise ratio, thus diminishing the overall link throughput. The solution to the issue is relatively well known, and relies on the so-called *wideband beamforming* technique—the subject of the next subsection.

C. Wideband Beam Steering

In the previous section, we have assumed that beam steering is implemented by applying a certain phase shift α_i at each radiating element of the FoA $i = 0, \ldots, NS-1$. The shift is computed requiring the beam center being steered from its natural position $(0, 0)$ to another position (θ_0, φ_0). The value of α_i is computed by elementary geometry assuming that the signal is monochromatic at the frequency f_0 [7]. This approach, as we have seen, fails when the signal bandwidth is relatively large. In this case, we need to apply, to the signal feeding the radiating element i, a *delay* equal to $\tau_i = \alpha_i/(2\pi f_0)$. This is tantamount to applying a different phase shift $\alpha_i(f)$ to different components of the signal spectrum: $\alpha_i(f) = 2\pi f \tau_i$, unlike the previous narrowband approach that keeps the phase shift constant across the spectrum ($\alpha_i = 2\pi f_0 \tau_i$).

With the wideband approach, the expression of the FoA factor is found to be

$$\zeta_{\mathrm{WB}}(\varphi, \theta; \varphi_0, \theta_0; \nu) = \Big| \underbrace{\zeta'_{\mathrm{WB}}(\varphi, \theta; \varphi_0, \theta_0; \nu)}_{\text{FoA factor}} \cdot \underbrace{\zeta''_{\mathrm{WB}}(\varphi, \theta; \varphi_0, \theta_0; \nu)}_{\text{array factor}} \Big|^2, \quad (9)$$

where

$$\zeta'_{\mathrm{WB}}(\varphi, \theta; \varphi_0, \theta_0; \nu) = \frac{\sin\left\{\pi\sqrt{S}\frac{\Delta}{\lambda}\left[\Omega(\theta) - \Omega(\theta_0)\right]\left(1+\frac{\nu}{f_0}\right)\right\}}{\sin\left\{\pi\frac{\Delta}{\lambda}\left[\Omega(\theta) - \Omega(\theta_0)\right]\left(1+\frac{\nu}{f_0}\right)\right\}} \times \frac{\sin\left\{\pi\sqrt{S}\frac{\Delta}{\lambda}\left[\Psi(\varphi, \theta) - \Psi(\varphi_0, \theta_0)\right]\left(1+\frac{\nu}{f_0}\right)\right\}}{\sin\left\{\pi\frac{\Delta}{\lambda}\left[\Psi(\varphi, \theta) - \Psi(\varphi_0, \theta_0)\right]\left(1+\frac{\nu}{f_0}\right)\right\}}, \quad (10)$$

$$\zeta''_{\mathrm{WB}}(\varphi, \theta; \varphi_0, \theta_0; \nu) = \frac{\sin\left\{\pi\sqrt{N}\frac{d}{\lambda}\left[\Omega(\theta) - \Omega(\theta_0)\right]\left(1+\frac{\nu}{f_0}\right)\right\}}{\sin\left\{\pi\frac{d}{\lambda}\left[\Omega(\theta) - \Omega(\theta_0)\right]\left(1+\frac{\nu}{f_0}\right)\right\}} \times \frac{\sin\left\{\pi\sqrt{N}\frac{d}{\lambda}\left[\Psi(\varphi, \theta) - \Psi(\varphi_0, \theta_0)\right]\left(1+\frac{\nu}{f_0}\right)\right\}}{\sin\left\{\pi\frac{d}{\lambda}\left[\Psi(\varphi, \theta) - \Psi(\varphi_0, \theta_0)\right]\left(1+\frac{\nu}{f_0}\right)\right\}}. \quad (11)$$

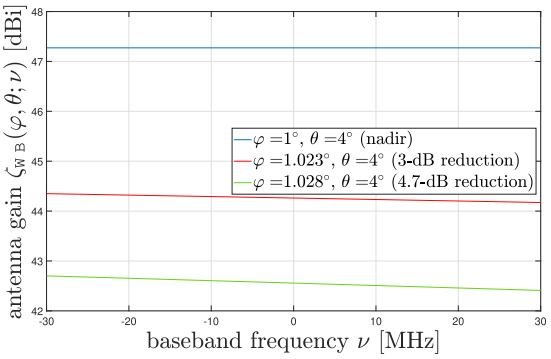

Fig. 7. Frequency selectivity of the FoA factor with wideband steering for a GEO configuration with $S = 1089$ and $N = 49$.

Comparing (9) with (1), we see that the only change is the shift of the beam center, so that the amount of selectivity for the wideband-steered beam is basically the same as in the case of the un-steered beam—very mild and negligible altogether. This is testified by Fig. 7 representing the very same cases as in Fig. 5, but with wideband beam steering implemented via appropriate true-delay array feeding—frequency selectivity is akin to what is experienced with the unsteered beam (Fig. 3). The same behavior can be observed for the LEO case, that we will not report here for the sake of brevity, as it is almost identical to what can be observed in Fig. 4. Of course, implementing a calibrated (wideband) delay, either at baseband or at intermediate frequency/RF, is more demanding than just implementing a calibrated phase-shift. A true wideband delay can be preferably implemented within a baseband digital beamforming network by processing each digital signal with a calibrated fractional-delay digital finite impulse response (FIR) filter—a well known structure in digital signal processing [37].

D. Hybrid Wideband-Narrowband Beam Steering

We have already mentioned in Section III-B that we can adopt different approaches to implement beam steering: Either at the formation level only, or at both at the formation and satellite level. We can take advantage of this possibility to devise smart, optimized *hybrid* architectures for wideband beamforming that was already envisaged in [3].

As already mentioned, frequency selectivity is generated by the large size of the formation (whilst the size of the individual satellite arrays is relatively small), so that the right choice is performing true wideband beamforming at the *formation level*, and applying simpler narrowband beamforming at the *satellite level*

$$\zeta_{\mathrm{H}}(\varphi, \theta; \varphi_0, \theta_0; \nu) = \Big| \underbrace{\zeta'_{\mathrm{WB}}(\varphi, \theta; \varphi_0, \theta_0; \nu)}_{\text{FoA factor}} \cdot \underbrace{\zeta''_{\mathrm{NB}}(\varphi, \theta; \varphi_0, \theta_0; \nu)}_{\text{array factor}} \Big|^2, \quad (12)$$

where $\zeta'_{\mathrm{WB}}(\varphi, \theta; \varphi_0, \theta_0; \nu)$ and $\zeta''_{\mathrm{NB}}(\varphi, \theta; \varphi_0, \theta_0; \nu)$ are given by (10) and (8), respectively.

This hybrid approach almost attains the same robustness of the FoA in terms of frequency selectivity as the previous

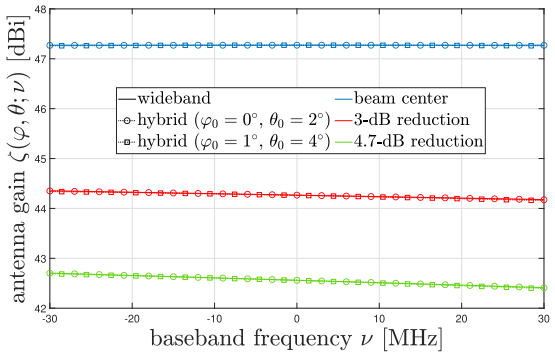

Fig. 8. Frequency selectivity of the FoA factor with hybrid steering (12) for a GEO configuration with $S = 1089$ and $N = 49$.

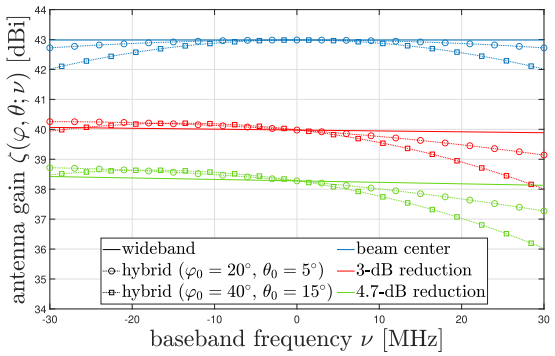

Fig. 9. Frequency selectivity of the FoA factor with hybrid steering (12) for a LEO configuration with $S = 9$ and $N = 2209$.

satellite-and-formation full wideband beamforming, with the advantage of reducing implementation complexity (in particular for the GEO case), thanks to satellite-level narrowband beamforming. This is testified by Fig. 8 showing the comparison between full and hybrid beamforming for the GEO case—no difference is seen within the full beamforming (solid lines) and the hybrid ones (the two configurations are represented by circular and square markers, which almost perfectly overlap with the solid lines, even in the case ($\varphi_0 = 1°$, $\theta_0 = 4°$), in which the beam is located at the edge of the coverage band).

For the LEO case, whereby the number of radiating elements is very large at satellite level and very few satellites are used, the hybrid approach is a bit less effective. Fig. 9 shows the performance of hybrid beamforming for a LEO FoA. This time the frequency selectivity is not perfectly compensated for as in the GEO case: The larger the departure of the beam center from the nadir ($\varphi = \theta = 0$), the more severe is in fact the effect of selectivity, as can be observed at ($\varphi_0 = 40°$, $\theta_0 = 15°$) (square markers) compared to the case ($\varphi_0 = 20°$, $\theta_0 = 5°$) (circular markers). However, it is still tolerable, as the variations are in the order of few dB.

As a final remark, it is pretty clear that all of our results in this section do *not* consider possible selectivity effects coming from the frequency response of the specific radiating element of the satellites' array—we concentrated here on the array/formation factor only.

IV. RANDOM THINNING OF A VERY LARGE FOA

A. Rationale of Formation Thinning

The main idea behind an FoA is clear: Realizing a very large equivalent antenna array taking advantage of the opportunity of satellite formation flying. The purpose of the large array is obtaining a very narrow beam with a footprint size similar to that of a cell of a cellular terrestrial network. Spacing between satellites helps reducing the requirements in terms of attitude control and even more important, as we will see in Section V-A, allows us to introduce space to deploy the solar arrays. Unfortunately, as noted in [3], the introduction of gaps between the arrays carried on-board each formation satellite produces undesired grating lobes in the FoA pattern. In addition, the introduction of some form of tapering through *formation thinning* (to be detailed later on) helps improving the control of near sidelobes without the need to operate peripheral satellites in transmit back-off (as would happen in conventional amplitude tapering).

The use of thinned and aperiodic arrays for active antennas has gained a growing interest in the last 20 years [38], [39], [40]. In such antenna architectures, uniform excitation allows all the amplifiers of the transmit active array to be operated under the same optimal condition, thus increasing amplifiers' efficiency while guaranteeing some degree of near sidelobe control.

Many array optimization techniques can be investigated and adopted to mitigate the level of grating lobes as well as of secondary emission close to the main lobe. Among them, *density tapering* [12], [41], [42] aims at emulating conventional amplitude-tapered arrays by adjusting the spacing of equi-amplitude fed radiating elements. Density-tapered arrays can obtain a significant reduction of the number of elements and avoid the needs for differently sized transmit amplifiers. In *thinned arrays* [13], [14], a significant part of the elements of a fully populated periodic array is removed maintaining the array beamwidth and controlling the radiation pattern in the sidelobe region. The selection of the elements to be retained can be performed according to a statistical method that takes decisions based on an assigned amplitude tapering to mimic [13], [14], or based on global optimization algorithms which aim at obtaining a reduction of the peak sidelobe levels [37], [43], [44], [45].

What we intend to pursue here is a simple approach that takes inspiration from the well-known concept of *statistically* thinned arrays [13], [14], elevated to the upper layer of the satellite formation: a *thinned FoA* (TFoA). In particular, starting from a very large number of *potential* satellite locations on a regular grid (with a potentially very narrow beam but an unsustainable number of spacecrafts), we adopt a probabilistic approach to perform thinning of the infeasible formation [13], [14] to come to a reasonable number of satellites: According to some rule, we mark many location as unoccupied, diminishing the actual number of satelites, but retaining the overall size of the formation. In so doing, the narrow beam feature is retained, the level of near sidelobes is reduced, and a suited (smaller) satellite count is attained. In particular, the FoA beam size remains

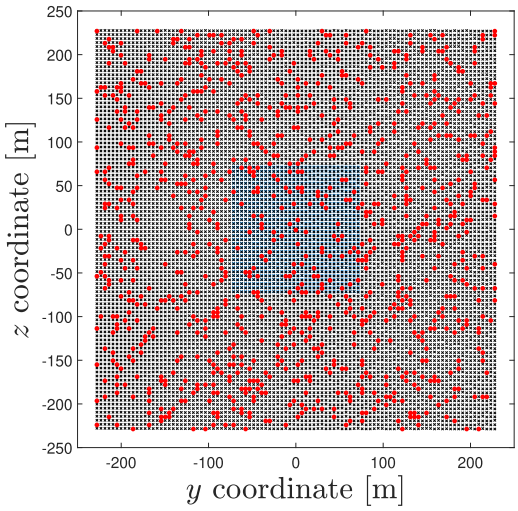

Fig. 10. Thinned formation with $\overline{S} = 1000$, $G_s = 100 \times 100 = 10\,000$, and $\delta = 0.1$. The grid spacing is $\Delta = 1.25\,L$ (Black: Potential grid locations; Red: Actual locations; Blue: Unthinned FoA with $S = \overline{S} = 1000$).

largely related to overall area occupied by the thinned FoA, while the beam peak gain depends on the actual number of satellites "survived" to the thinning exercise. According to the theory developed for *statistically thinned arrays* [12], the near sidelobes of the TFoA factor approximate the near sidelobes of the seeding amplitude tapering used as reference distribution for the statistical thinning.

To understand our approach, we start with a specific example, reported in Fig. 10, assuming a full square grid with the usual regular spacing $\Delta = 1.25\,L$ in both directions (see [3] for further justifications on this setting), and with $G_s = 100 \times 100 = 10\,000$ *potential* locations for our FoA satellites (represented by the tiny "×" black markers in Fig. 10). The actual occupation of a certain location by one satellite is randomly chosen according to a certain probability function: in particular, the occupancy of location s, $s = 1, \ldots, G_s$, is a *binary random variable* (0=unoccupied, 1=occupied) ξ_s with $\Pr\{\xi_s = 1\} = q_s$ (and of course $\Pr\{\xi_s = 0\} = 1 - q_s$). By doing so, the (actual) number of satellites in the formation $S = \sum \xi_s$ is a random variable whose average value is $\overline{S} = \mathbb{E}\{S\}$. To regulate the (average) number of satellites in the FoA after thinning, we set $q_s = \overline{S} \cdot \rho_s = \delta \cdot G_s \cdot \rho_s$, where $\delta = \overline{S}/G_s$ is the desired satellite "density" on the grid (determined by the desired average number of satellites $\overline{S}$), and where $\rho_s \geq 0$ is a suitably selected normalized[3] tapering function such that $\sum \rho_s = 1$. For instance, we may assume uniform tapering, i.e., $\rho_s = 1/G_s$, and that all locations are drawn independently of each other. In this case, the number of satellites in the formation S turns out to be a *binomial random variable* whose average value is (by construction) $\overline{S} = \mathbb{E}\{S\} = \delta \cdot G_s$ – starting from a $G_s = 10,000$ grid and assuming $\delta = 0.1$, we get an average number of satellites in the formation equal to $\overline{S} = 1000$ that may be sustainable—the overall size (contour) of the formation still being as large as that of the original square grid. Fig. 10 depicts an example of a particular draw of such a thinned formation (the total number of satellites is 987), with the occupied locations represented by the red dots. For the reader's convenience, Fig. 10 also reports in blue the locations of a hypothetical unthinned FoA [3] bearing the same spacing $\Delta = 1.25\,L$ and the same number of (average) satellites, $S = \overline{S} = 1000$.

What is the effect of the random thinning of satellites? The direction of maximum array gain will still be $\varphi = 0, \theta = 0$ irrespective of the particular draw, and the FoA gain will still be proportional to the actual number of satellites S. When G_s is very large (as in our example above), by the law of large numbers the (random) value of S will be always very close to $\overline{S} = \delta G_s$.

The semi-random position of FoA satellites, while not affecting the direction of peak gain value, enables the utilization of a more compact periodicity in the underlying regular grid. This results in periodic grating lobes corresponding to $\sin(\theta)$ positions multiples of $\frac{\lambda}{\Delta}$. Specifically, in configurations where $\Delta = 1.25\,L$, this approach effectively prevents the generation of adjacent grating lobes present in the configuration with $\Delta = 4\,L$. In addition, the thinned configuration follows main beam and near sidelobes of the originating full aperture. The width of the main lobe is similar, yet a bit smaller compared to the case of the full grid, since it is dictated by the maximum size of the formation, that is almost unchanged in spite of the random satellite placement (please see Section V-B for a specific comparison).

B. FoA Thinning Examples

A first example of a TFoA performance can be seen in Fig. 11 depicting the formation array factor of the uniform-probability TFoA introduced above (compared to that without thinning), where the narrow beam and low sidelobes features can be easily noticed. For a fair comparison, Fig. 11 also reports the pattern obtained with the *unthinned* configuration [3], using $\Delta = 1.25\,L$ (green line) and $\Delta = 1.25\,L/\sqrt{\delta} \approxeq 4L$ (blue line), respectively, where the latter case is considered because it spans the same area occupied by the TFoA ($\sqrt{\delta}$ is due to the squared shape of the formation—see also Fig. 10 for a pictorial representation of the different span sizes). In all cases, the total number of satellites is the same, and this is the reason why we get the same array gain at the nadir. However, in the case of $\Delta = 1.25\,L$, we observe a larger main lobe due to a smaller area spanned by this FoA configuration. On the other side, when considering $\Delta = 4\,L$, the main lobe becomes comparable with that offered by the thinned FoA (TFoA), but the unwanted grating lobes becomes clearly visible.

Different thinning strategies with nonuniform probability can also be devised, trying to improve on the issue

[3]Care must be taken in selecting the tapering function. When the density δ is high (i.e., $\overline{S}$ is close to G_s) and the tapering rule is "peaky," it may turn out that $q_s > 1$ for some s. This condition leads to *unfeasible* probabilistic thinning and has to be prevented in advance: $\max\{\rho_s\} \cdot \overline{S} \leq 1$.

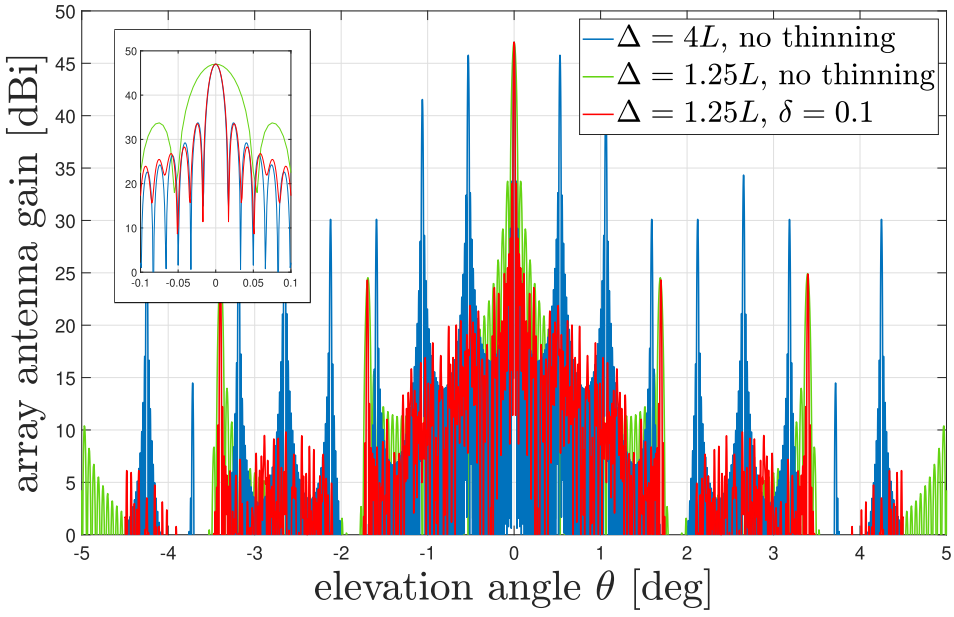

Fig. 11. Array factor of a GEO FoA with $S = 1024$, $N = 49$ (Blue: Regular squared array, with $\Delta = 4\,L$; Green: Regular squared array, with $\Delta = 1.25\,L$; Red: Thinned array with $\delta = 0.1$, $G_s = 10,000$, and $\Delta = 1.25\,L$).

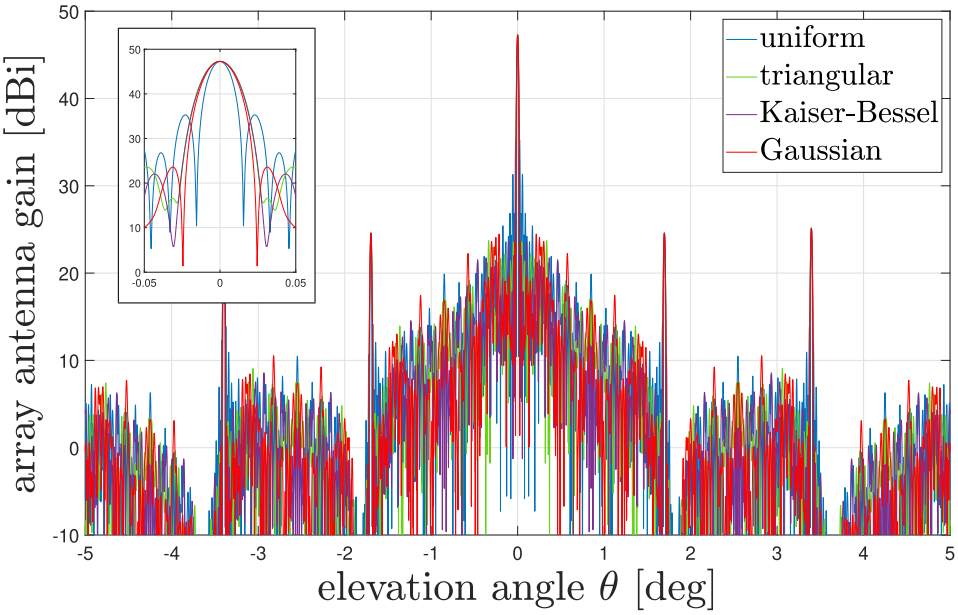

Fig. 12. Array factor of a GEO FoA with $\overline{S} = 1089$, $N = 49$ with different tapering distribution – Blue: Uniform; Green: Triangular; Purple: Radial Kaiser-Bessel, $\alpha = 9$; Red: Radial Gaussian, $\sigma_s = \sqrt{G_s/32}$, with $G_s = 10\,000$.

of sidelobe reduction. We can vary in fact the value of q_s from the center to the edges of the grid so as to implement a kind of "probabilistic tapering" on the formation (e.g., triangular tapering on both main directions). An example is shown in Fig. 12 with triangular tapering (green line). For comparison, the array factor in the case without tapering is also reported with the red line. It is seen that the main beam is practically stable, and that the secondary emission is always bounded to less than -20 dB from the maximum gain. In particular, the secondary emission close to the main lobe is "cleaner" in the tapered FoA, thus creating a smaller amount of interbeam interference in a closely-spaced multibeam communications network.

Optimization of the thinning (probabilistic) rule is outside the scope of this article. We just report in Fig. 12 the results in terms of FoA factor of both (truncated) radial Gaussian and Kaiser-Bessel thinning with different values of the density parameter δ, for which, respectively

$$\rho_{s,\mathrm{G}} = \frac{1}{Q} \exp\left\{-\frac{\left(y_s^2 + z_s^2\right)}{2\sigma_\rho^2}\right\}, \tag{13}$$

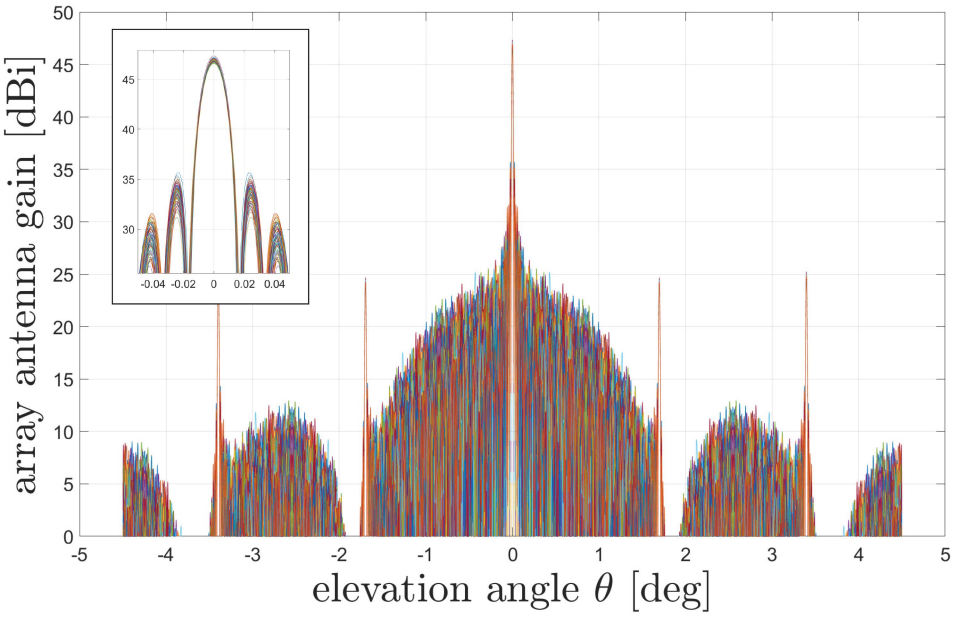

Fig. 13. Array factors of independent FoA draws as in Fig. 11.

$$\rho_{s,\mathrm{K-B}} = \frac{1}{Q'}\,\mathrm{I}_0\left(\alpha\sqrt{1-\frac{(y_s^2+z_s^2)}{(L/2)^2}}\right), \qquad (14)$$

where Q and Q' are suited normalization factors so that $\sum \rho_s = 1$, the values (y_s, z_s) are the coordinates of the sth grid point, σ_ρ^2, α regulate the sharpness of the Gaussian tapering function, and I_0 is the modified Bessel function of the first kind and order zero. The effect of tapering is pretty clear: The width of the main lobe of the FoA emission (i.e., its aperture) is increased by tapering, but the level of the near sidelobes is greatly reduced as well, thus contributing to decrease interbeam interference to neighboring beams. The example is not 100% realistic, since the obtained aperture leads to a beam size on Earth from GEO orbit that is very small—its intention is only to show the use and applicability of thinning to our FoA.

The probabilistic approach that we follow is particularly effective for formation of arrays (FoAs) involving a large (average) number of satellites $\overline{S}$. In this case in fact, any randomly-chosen configuration within the grid (any draw) features $S \simeq \overline{S}$ and works as well as any other by the law of large numbers. This is testified by Fig. 13 reporting the array factor of many different independent draws of a tapered FoA as in Fig. 11. To better appreciate the behavior of the main lobe, the inset reports a magnification around the main lobe.

Probabilistic thinning is also expedient to meet possible spacing or configuration requirements of the formation coming from the satellite design. In the next section, we will see that optimum power generation may call for side- or top-mounted solar arrays, the consequence of this being the necessity of certain constraints on satellite location and orientation in the FoA. The smartest approach to enforce this is, again, assuming a full grid with the prescribed intersatellite spacing, and introducing special criteria to "populate" the FoA according to a fixed thinning probability and to further simple configuration constraints.

C. Robustness Against Calibration and Array Geometry Errors

When deploying an FoA (thinned or unthinned), a major issue is represented by inaccurate positioning of the spacecrafts, with possible impact on the FoA radiation pattern (1). To understand the pattern sensitivity to possible position errors of the diverse FoA satellites, we introduce a random offset $\boldsymbol{\delta}_s = [\delta_{s,x}, \delta_{s,y}] \in \mathbb{R}^2$ that adds up to the coordinates of the sth satellite to model the effect of such inaccuracy/instability.

Fig. 14 shows the sensitivity of the uniformly-thinned FoA factor to position accuracy for a given random realization of the satellite locations—Fig. 14(a) reports the SA center locations, whereas Fig. 14(b) shows the array antenna pattern as a function of the elevation θ. Each plot is computed assuming a random realization with $\overline{S} = 1000$, (i.e., $q_s \equiv \delta = 0.1$), and both $\delta_{s,x}$ and $\delta_{s,y}$ to be Gaussian-distributed random variables (RVs) with zero mean and standard deviation σ: The case $\sigma = 0$ (black dots/lines) represents the case with perfect control of satellite localization, whereas red and blue dots/lines represent the cases $\sigma = 0.15$ m and $\sigma = 10$ m, respectively.[4] As expected, black and

[4]Given the system parameters considered throughout the article, and notably those used in this section (spacing across the satellites equal to 0.92 m), the first case is selected to avoid overlapping across SAs. The

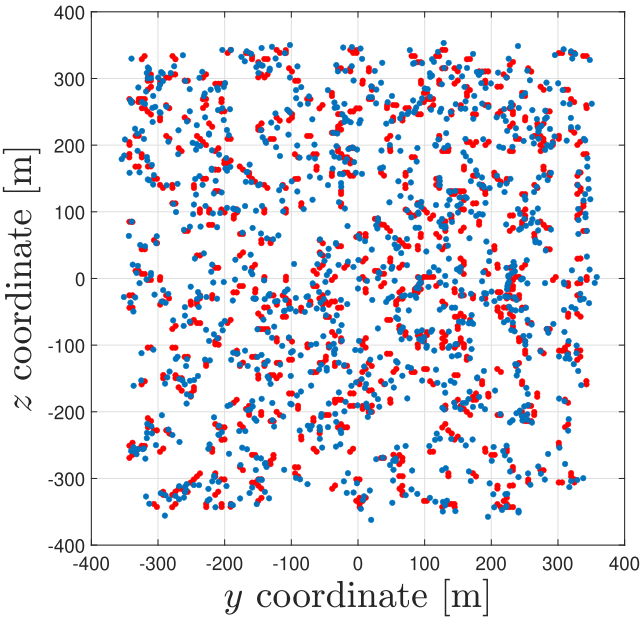

(a)

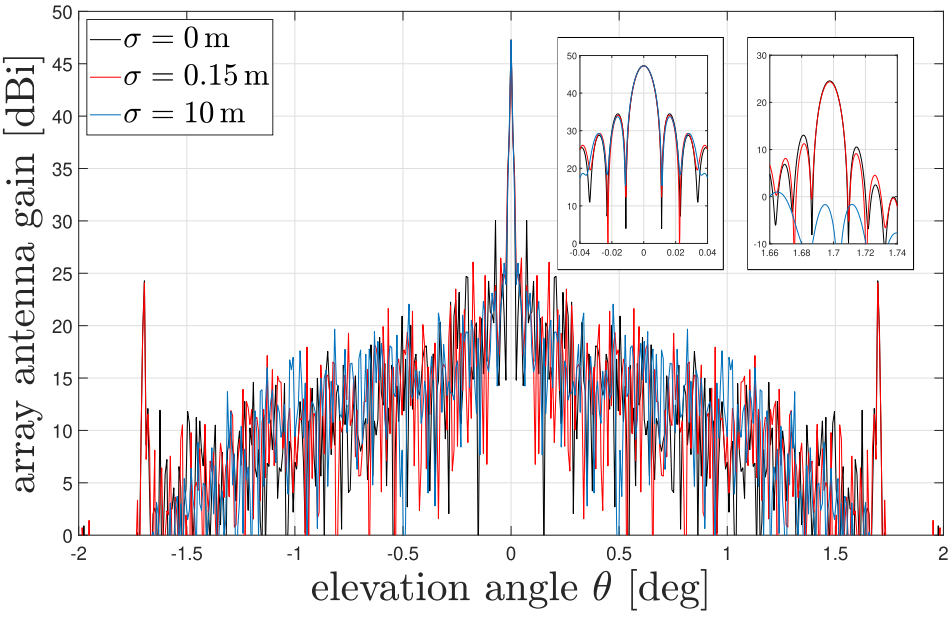

(b)

Fig. 14. Sensitivity of the thinned array to random satellite position errors. (a) Coordinates. (b) Antenna pattern.

red dots and lines are practically indistinguishable. More interestingly, in the case $\sigma = 10\,\text{m}$, although the location of the satellites changes noticeably, there is no significant difference in the array pattern, especially concerning the main lobe and the sidelobes (please see the insets), whereas the grating lobes in this particular realization are somewhat unaltered from the random satellites' locations. The gap with respect to the main lobe is around 25 dB for the nadir-looking beam (therefore, barely affecting the pattern in terms of interbeam interference for limited scanning angles). The grating-lobe suppression is dictated by the satellite array factor. Note that Fig. 14 considers only *one* random realization per value of σ. By performing many trials with independent realizations, it can be observed that the side-lobe envelope follows the satellite array factor.

The same conclusion can be derived when considering errors related to the RF chains calibration, causing inter-satellite random phase shifts. Fig. 15 shows the sensitivity of the FoA pattern gain to phase inaccuracy, wherein each

second case does generate possible overlapping across adjacent SAs: however, this situation can be solved by displacing the satellites over different planes along the x axis (see Fig. 2), a few meters away from each other, as the array pattern is not affected by different x coordinates, as illustrated in [46].

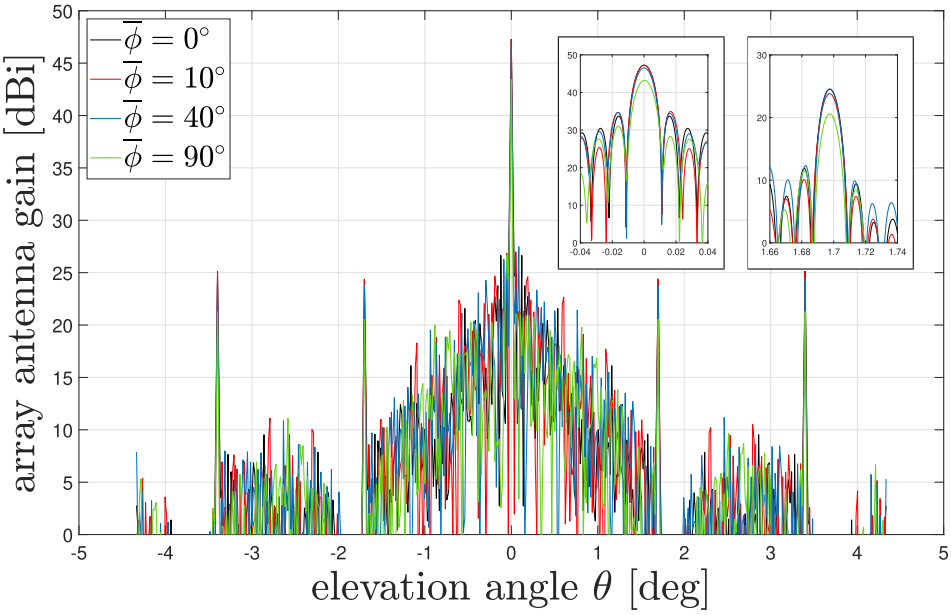

Fig. 15. Sensitivity of the thinned array to inter-satellite random phase errors.

plot is computed assuming that each SA's phase shift is uniformly distributed in $[-\overline{\phi}, \overline{\phi}]$, with $\overline{\phi} = 0°$ (black line) representing the case with perfect calibration. The other cases represent increasing instability with $\overline{\phi} = \{10°, 40°, 90°\}$ shown in red, blue, and green lines, respectively. Similarly to Fig. 14, please note that only *one* (typical) random realization per value is considered. Even in this case, the impact of miscalibration on the array pattern gain is not disruptive when $\overline{\phi} < 40^o$.

V. FOA CONFIGURATION FOR OPTIMAL ELECTRICAL POWER GENERATION

A. Interplay of Solar and Antenna Arrays

The demand in terms of electrical power of the FoA is of course a challenge in itself. The simplest arrangement is integrating the solar cells and the radiating elements in a dual-face antenna/solar generator panel with radiating elements on the side facing the Earth and with solar cells on the other side. Such arrangement, dubbed *body-mounted*, turns out to be *inefficient* since such a GEO satellite would always point towards the same spot on Earth, therefore periodically changing the solar panel pointing wrt the Sun. More importantly, the solar panel mounted on the back side of the active antenna will be completely shadowed from the Sun rays for half of its orbit.

Let us compare this arrangement with that of a conventional GEO communication satellite adopting: 1) off-body SGs following the Sun orientation by means of a dedicated SADM; plus 2) a body-mounted fixed antenna pointed towards the Earth. It turns out that the satellite with body-mounted solar generators goes through an extended eclipse period of about 12 hours per day as compared to the much shorter eclipse lasting no more than 70 minutes (and only occurring during three weeks before and three weeks after the summer and winter solstices [47]) of the conventional Sun-facing GEO satellite. The longer and more frequent total eclipses call for a much bigger battery capacity (hence, onboard weight) required to power the satellite payload during the long darkness time. In addition, the much higher number of charge/discharge battery cycles tends to reduce their lifetime unless the depth of discharge (DoD) is reduced. In other words, being the satellite platform attitude dictated by the communication requirements, a body-mounted SG solution is largely suboptimum in terms of the solar array surface yield.

A way out of this is to assume a more conventional configuration of each FoA satellite, in particular placing the SG at the side of the main (fixed) array antenna, with the capability to keep the panel always oriented towards the Sun by means of an appropriate SADM, so as to limit the duration of daily (partial) eclipses. Of course, this approach leads to specific constraints on the placement and orientation of spacecrafts in the FoA. To better understand the FoA eclipses' specific issues one can refer to Appendix A, providing a detailed analysis of this phenomenon. In a nutshell, even when using a SADM for the FoA, the SGs will experience a (partial) eclipse twice per day. This happens when some FoA satellite, or another SG body close to the SG of interest, is shadowing the Sun rays. The duration of the eclipse is clearly depending on the FoA geometry. As shown in Appendix A, worst-case shadowing occurs when one SG is masking the adjacent SG. This is because the (inclined) SA body casts a smaller shadow than the (parallel) nearby SG during the eclipse period. To limit the duration of the SG-induced eclipse, it is necessary to keep an empty grid slot between two adjacent SGs in the formation. In addition, to keep the solar radiation as orthogonal as possible to the SG plane, the SADM should rotate it along the Earth north–south axis. These two constraints must be incorporated into the criterion to perform FoA thinning already discussed in Section IV.

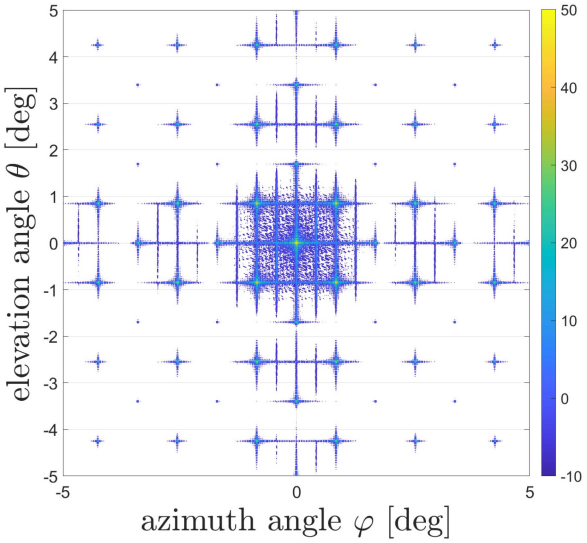

Fig. 16. 2-D map of the antenna gain for the unthinned GEO FoA chessboard geometry array factor ($S = 1089$, $N = 49$, $\Delta = 1.25\,L$).

The situation for a LEO satellite is less critical: we have one eclipse per orbit, but its overall duration is much shorter than for the GEO case, requiring a relatively small battery capacity (independent of the kind of mounting of solar arrays)—as shown in [48] the maximum eclipse duration is 35 min, and its fixed solar array power conversion efficiency is reduced by the time-variant sunlight incidence angle. In the following, we will concentrate on the criteria to optimize a GEO FoA only.

B. Power-Generation Optimized Thinned FoA Geometry

The general FoA thinning approach described in Section IV must be aligned with the findings from Section V-A to make the FoA compatible with the SG constraints explained above. As a first step, we consider the presence of the SGs on top of the main body-mounted array antenna, assuming that the satellite body and the SGs both occupy a "box" of the same size, so that *two* locations in our virtual FoA grid would now be occupied by a single satellite. This assumption limits the possible SA positions in the grid, taking into account that now only *half* of them are available. When no thinning is adopted we obtain a "chessboard" FoA geometry that provides the antenna gain depicted in Fig. 16. This FoA geometry shows a poor grating lobe performance, particularly along the $\theta = \varphi$ axis due to the SA chessboard geometry causing the increased SAs spacing.

A possible approach to populate the FoA respecting the criteria illustrated in Section V-A while randomizing its geometrical configuration is starting from a virtual regular square grid of 2×2 *boxes*, each box hosting up to 2 spacecrafts. Selecting random position in each box, the chessboard configuration is avoided, and the FoA secondary lobe level (even for a low degree of thinning, i.e., $q_s > 0.5$) is greatly improved. However by just selecting random position/orientation of any satellites in each box does not necessarily lead to configurations complying with the SGs geometrical constraints. For instance, the SGs shall rotate along the Earth north–south axis, and two SGs have to keep a distance greater than Δ along the axis orthogonal to the previous one. Therefore, we also have to take into account the SA position inside a single box, how each box interacts with the neighboring ones, to satisfy the above constraints during the FoA construction.

Fig. 17. Possible SA configurations into any grid box.

Specifically, the FoA is sequentially populated starting from an empty grid of boxes, and considering all of the possible boxes one by one. When a box, according to a certain probabilistic thinning rule, is considered to be occupied, the location/orientation of the satellites in the box is randomly selected in a subset of 6 possible configurations (see Fig. 17). The selected configuration may or may not be acceptable, since: 1) the SGs can only sit on the top or on the bottom of the SA to be able to correctly operate the SADMs; and 2) the SGs of the current satellites box must not be immediately adjacent to any other SGs from other occupied boxes. Enforcing such constraints leads to a final acceptable FoA configuration.

A significant result of such procedure is shown in Fig. 18, reporting the worst-case $\theta = \varphi$ cut of the nontapered TFoA pattern for different values of the (uniform) thinning probability q_s. The plot is obtained with a constant final number of SAs $S = 1089$. This means that the original grid of virtual positions is of different size for each q_s value. The improvement in terms of grating lobes and more in general sidelobes is apparent. For the reader's convenience, Fig. 18 also contains a magnification around the main lobe, to emphasize the effect of thinning. The whole array pattern as a function of φ, θ is also shown in Fig. 19 for $q_s = 0.6$ and with $S = 1089$ SAs.

C. FoA Power Subsystem Analysis

The diverse FoA configurations that are obtained with the constrained thinning procedure above have been verified by an accurate system analysis. In particular, a complete power subsystem simulation based on the power energy platform simulation (PEPS) tool [49] was carried out, taking into account solar arrays, batteries, and power electronics subsystems, as well as accurately modeling the single SA orbit. As already mentioned, the R-GEO configuration envisaged in [3], albeit practical, faces a 12-h eclipse per day as each satellite's array antenna pointing to the Earth masks the SG laying on the opposite array side. As a result, even

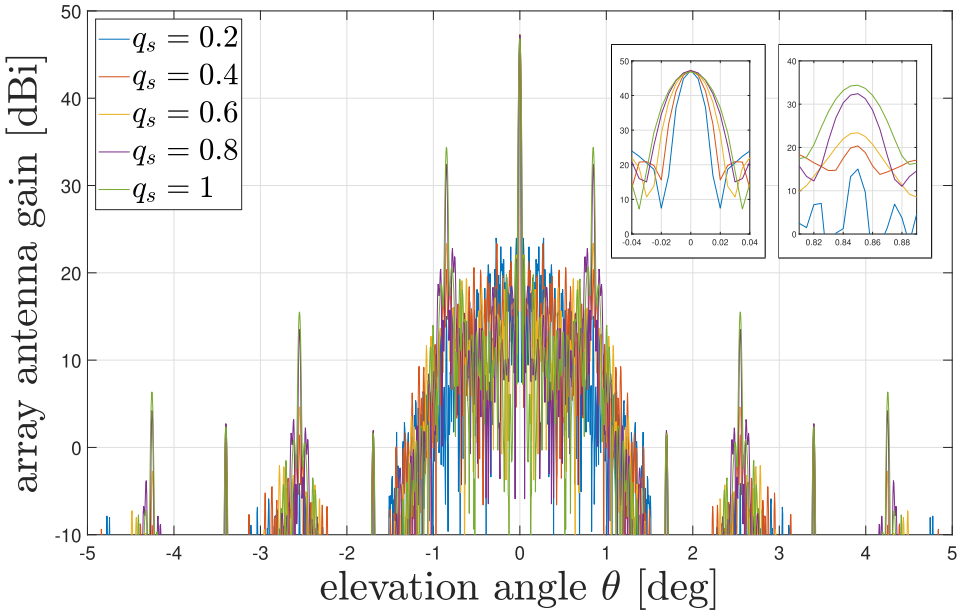

Fig. 18. GEO FoA worst-case ($\theta = \varphi$ plane) array factor for different values of the thinning probability q_s ($S = 1089$, $N = 49$ and $\Delta = 1.25\,L$).

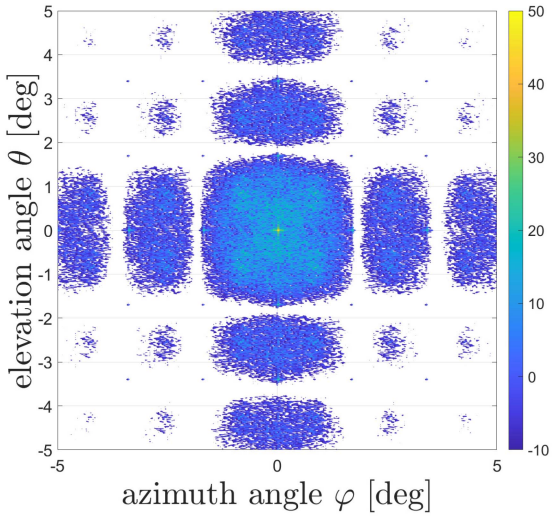

Fig. 19. 2-D map of the antenna gain for the GEO FoA array factor for $q_s = 0.6$ ($S = 1089$, $N = 49$ and $\Delta = 1.25\,L$).

TABLE II
Power Subsystems Assumptions and Simulation Results

Parameter	*R-GEO*	*LEO*	*Unit*
Orbital altitude	35, 786	550	km
Mission lifetime	5	5	years
Percentage of time the Satellite is active	100	70	%
Solar array calculated Temperature uncertainty	10	10	°C
Solar array mounting technique	SADM	body-mounted	
Solar generators total surface	11.70	12.96	m^2
Single eclipse duration	3.14	0.59	hours
Average SG illuminated Surface during eclipses	50	0	%
Number of eclipses/day	2	1	
Number of cycles charge/discharge	4, 100	29, 200	
Battery depth of discharge	80	38	%
Battery weight	59	52	kg
Baseline platform power consumption	257	257	W
DC power available for the payload	1, 643	993	W

with 52 kg of batteries on board each FoA satellite, the average power for the payload is limited to about 200 W, which is insufficient for the targeted mission. For the GEO case, we will therefore focus on a SA architecture featuring a side-mounted SADM-SGs, while still retaining the body mounted SG option for the LEO case (wherein the eclipses duration is much shorter).

For the R-GEO FoA, the eclipse duration and the corresponding SGs worst-case average power are computed in detail as reported in Appendix B. Our assumptions about the power subsystem are summarized in Table II for a SADM-equipped R-GEO satellite, as well as for a simpler LEO with body-mounted SG. For the R-GEO, the number of eclipses is the sum of the 3650 FoA self-induced plus 450 seasonal GEO standard eclipses occurring over an assumed five-year lifetime. For the R-GEO eclipses, we take the worst-case average SG efficiency from Table IV (Appendix B), in a time frame covering both the equinoxes and self-induced eclipses.

The results of the PEPS simulations are summarized in Figs. 20 and 21 and Table II, allowing us to derive a relatively accurate payload power budget.

We also derive a realistic estimate of the payload power consumption as shown in Table III, taking into account state-of-the-art space-segment technologies. As is known, semiconductor technology represents the fundamental component of the on-board digital processor (OBP) and any advance in the manufacturing process corresponds to an improvement of the digital payload performance (i.e., power consumption, speed, throughput processing density, volume, integration, etc.). Considering the projected timeframe of the development, ultradeep submicron (UDSM) technology is expected to be available, and FinFET (<

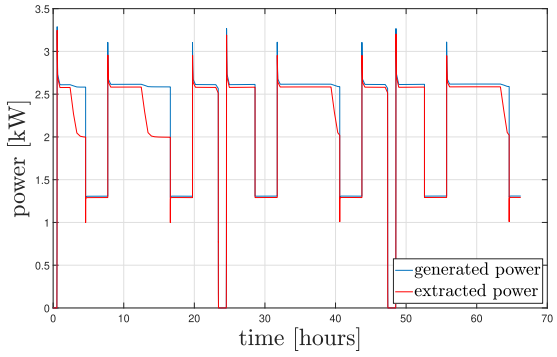

(a)

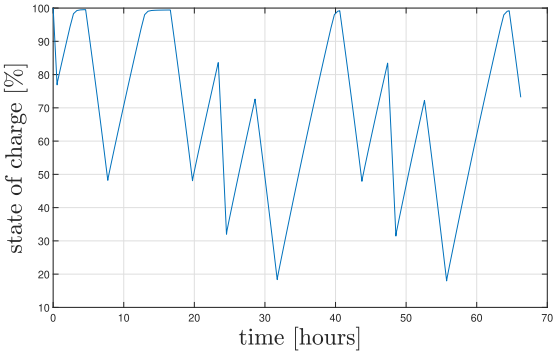

(b)

Fig. 20. Simulated power generation for the R-GEO case using SADM SG and ad hoc thinned FoA for the worst case corresponding to equinoxes, plus self-induced bi-daily eclipses. (a) Power generation. (b) Battery depth of discharge.

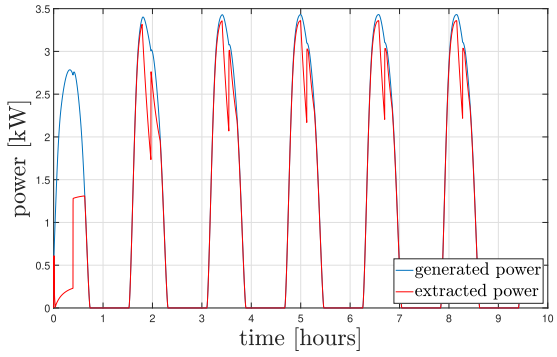

(a)

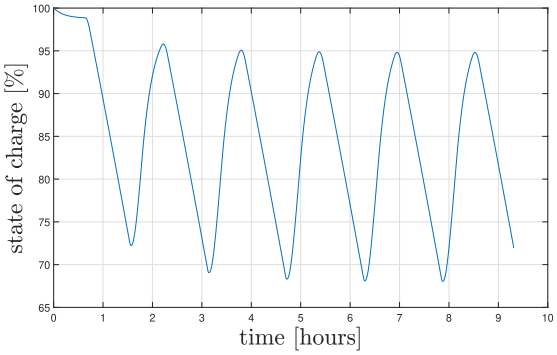

(b)

Fig. 21. Simulated power generation for the LEO case using a body-mounted SG for the worst case eclipse period. (a) Power generation. (b) Battery depth of discharge.

TABLE III
Payload DC Power Consumption Analysis

Parameter	*R-GEO*	*LEO*	*Unit*
Number of array elements/SA	49	2209	
User bandwidth	60	60	MHz
Digital processor (FWD+RTN) Power consumption	50	350	W
RF receive front-end DC power consumption	5	220	W
ISL power consumption	40	10	W
Simulated DC power available for the payload	1643	993	W
Available DC power for the RF transmit front-end	1548	414	W
Transmit section DC-to-RF power conversion efficiency	35	35	%
Available SA RF transmit power	542	145	W

7 nm) technology is considered for the OBP power consumption estimates. FinFET nanoelectronic semiconductor technology is expected to overcome the limitations of current on-board digital processing capabilities, enabling in-space processing with capabilities similar to current terrestrial microelectronics state-of-the-art [50]. As shown in Table III, the results for the available SA RF transmit power depend on the the dc-to-RF power conversion efficiency, that has been estimated to be of about 35% for state-of-the-art S-band solid-state power amplifiers (SSPAs) in multicarrier operation. It is worth noting that, in comparison to previously reported high-level analyses provided in [3, Table II], current refined platform design and power analysis indicates an increase of available SA RF transmit power for the GEO case, and a decrease for the LEO case.

VI. CONCLUSION

In this article, we have taken into consideration the recently-proposed FoA technology, extending previous analyses and taking into consideration important design/implementation aspects, namely: 1) the large direct radiating antenna (DRA) frequency selectivity and countermeasures; 2) the applicability of array thinning techniques to reduce the number of satellites required to achieve a given beam size; and 3) the onboard power generation strategy as well as the associated optimal geometrical configuration taking into account antenna and solar generator design constraints. This allowed us to derive more realistic results about the satellites power subsystem, the payload power consumption, and the antenna pattern taking into account system-optimized configurations.

It was found that, owing to the very large FoA size and number of elements (i.e., satellites), the use of phase-only (narrowband) beamforming may cause major frequency selectivity impairments. This issue can be solved by resorting to wideband or hybrid wideband/narrowband beamforming. In particular, for a GEO FoA, narrowband beamforming can be safely used in each satellite array antenna, leaving the adoption of wideband beamforming at the formation level only. Array thinning was shown to be an effective approach

Fig. 22. Illumination by the Sun of a GEO FoA.

to keep the beam size as narrow as that of the unthinned array while reducing the number of SAs and increasing their average distance. This goes together with a reduction of the FoA peak gain proportional to the thinning density. A detailed analysis of the satellite power subsystem showed that the body-mounted solar generator option is only applicable to the LEO case. In the GEO case, a steerable solar generator is required to limit the duration of eclipses. Unlike conventional GEO satellites, the FoA geometry combined with individual SG per satellite is not sufficient to avoid the bidaily eclipses. A specific FoA geometry based on a constrained chessboard-based thinning approach allowed us to satisfy the SG requirements keeping an acceptable antenna pattern.

Future work will be dedicated to analyze in detail the system throughput taking into account a more detailed system model, a realistic traffic distribution, a strategy for radio resource management, and optimized payload configurations. The goal is to extend the beamforming-based optimization approach adopted in this article to a more advanced but challenging massive multiple input multiple output (MIMO) configuration as was done in [24], [25], and [26] for a Ka-band broadband satellite access network.

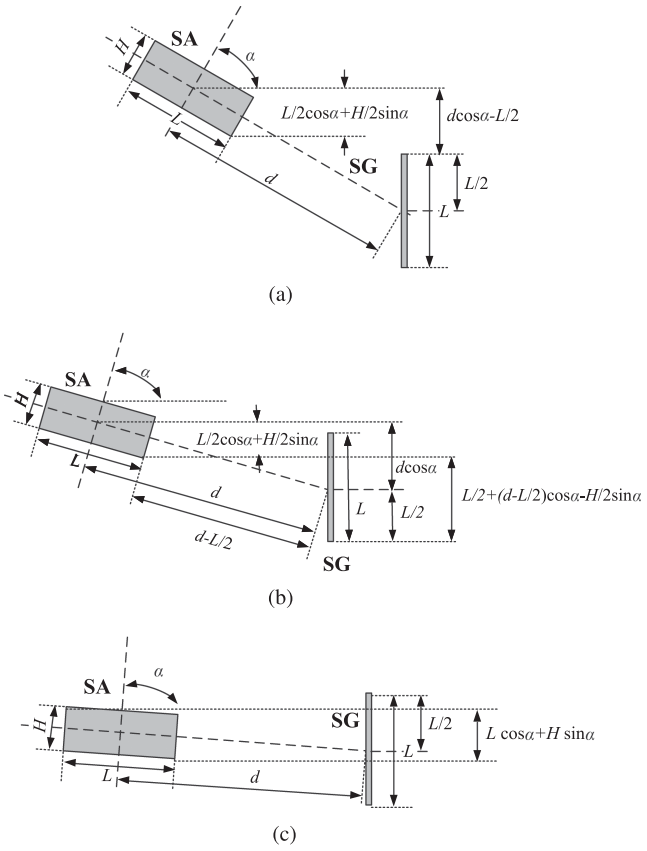

Fig. 23. Shadowing of the SG by a neighbor satellite's SA in a GEO FoA before and during the eclipse. (a) Before the eclipse start. (b) During the partial SA-induced eclipse. (c) During the full-SA induced eclipse.

APPENDIX

A. Eclipse Analysis

In this appendix, we analyze the FoA SG's eclipse which, as mentioned before, is quite different from the one typically experienced by (single) GEO/geosynchronous Earth orbit (GSO) satellites [46]. This is because the SAs and the attached SGs are shadowing the SG next to them when the FoA is in certain arc of the GEO orbit characterized by a relatively small angle between the FoA plane and the Sun-rays direction, as shown in Fig. 22. To compute the angle at which the (partial) eclipse starts, we have to consider the following two possible cases.

1) The left SA lower body part is getting aligned to the right SG upper border [see Fig. 23(a)].
2) The left SG lower body part is getting aligned to the right SG upper border [see Fig. 24(a)].

The two different cases have to be carefully considered one at a time.

1) *Eclipse Analysis SA-SG:* Looking at Fig. 23(a), we can see that the vertical distance between the SA body lower border and the SG upper part is given by

$$\Delta(\alpha) = d\cos\alpha - \frac{L}{2} - \left[\frac{L}{2}\cos\alpha + \frac{H}{2}\sin\alpha\right]. \quad (15)$$

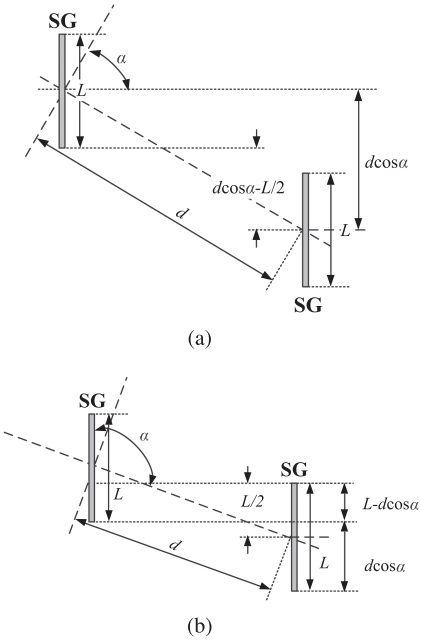

Fig. 24. Shadowing of the SG by a neighbor satellite's SG in a GEO FoA before and during the eclipse. (a) Before the eclipse start. (b) During the eclipse.

Therefore, the FoA SG eclipse starts at the angle α_1 such that $\Delta(\alpha_1) = 0$. This condition is verified when

$$(2d - L)\cos\alpha_1 - H\sin\alpha_1 - L = 0. \tag{16}$$

The partial SA body shadowing on the SG continues until the angle α_2 for which the full SA body shadows the SG is reached. Looking at Fig. 23(b) this condition is found as

$$(2d + L)\cos\alpha_2 + H\sin\alpha_2 - L = 0. \tag{17}$$

The SA induced SG partial eclipse is then starting as shown in Fig. 23(b) to then become a full SA body induced eclipse as shown in Fig. 23(c).

The size $L_{\text{eff}}(\alpha)$ of the SG section that turns out to be illuminated by the Sun in the first quarter of the orbit can be computed as

$$L_{\text{eff}}(\alpha) = \begin{cases} L, & \text{for } \alpha \le \alpha_1 \\ \left(d - \frac{L}{2}\right)\cos\alpha - \frac{H}{2}\sin\alpha + \frac{L}{2}, & \text{for } \alpha_1 < \alpha < \alpha_2 \\ L\,(1 - \cos\alpha) - H\sin\alpha, & \text{for } \alpha_2 \le \alpha \le \pi/2. \end{cases} \tag{18}$$

For $\pi/2 < \alpha \le \pi$, a symmetric situation occurs.

2) *Eclipse Analysis SG-SG:* The eclipse geometry for this case is much simpler as the SGs are both orthogonal to the sunlight rays' direction. Looking at Fig. 24(a), it is easy to see that in this case the vertical distance between the SG lower border and the SG upper part is given by

$$\Delta(\alpha) = d\cos\alpha - L. \tag{19}$$

The eclipse in this case begins at the angle

$$\alpha_1 = \cos^{-1}\left(\frac{L}{d}\right). \tag{20}$$

Also looking at Fig. 24(b), we see the size $L_{\text{eff}}(\alpha)$ of the SG section that turns out to be illuminated by the Sun in the first quarter of the orbit is

$$L_{\text{eff}}(\alpha) = \begin{cases} L, & \text{for } \alpha \le \alpha_1 \\ d\cos\alpha, & \text{for } \alpha_1 \le \alpha \le \pi/2 \end{cases} \tag{21}$$

with, as before, a symmetric situation when $\pi/2 < \alpha \le \pi$. We are now in a position to derive the duration (in hours) of a single eclipse

$$T_{\text{ecl}} = 12\left(\frac{\pi/2 - \alpha_1}{\pi/2}\right). \tag{22}$$

B. Eclipse Analysis Results

To derive the so-called *profile* of the illuminated size SG $L_{\text{eff}}(\alpha)$ as a function of α, we assume $L = 3.68$ m, $H = 0.8$ m, and a minimum normalized SG edge spacing of $1.25 \cdot L$ (i.e., just one empty slot between the SG-SA and the SG). This leads to $d = 2.5 \cdot L = 9.2$ m. The empty slot is required to avoid an exceedingly long eclipse and a consequent excessive battery discharge. By solving (16), (17), and (20), we get the results reported in Table IV. The SG side tile reduction during the eclipse is plotted in Fig. 25. We see that the SG-SG shadowing case represents a worst-condition in terms of eclipse duration, shadowed surface, and consequently average power collected by the SG.

TABLE IV
FoA Eclipse Analysis Results

Parameter	*SA-SG case*	*SG-SG case*	*Unit*
α_1	72.43	66.42	degrees
α_2	82.49	n/a	degrees
T_{ecl}	2.34	314	hours
$\mathbb{E}\{L_{\text{eff}}(\alpha)\}$	2.88	1.87	m
SG average efficiency during eclipse	78.18	50.71	%

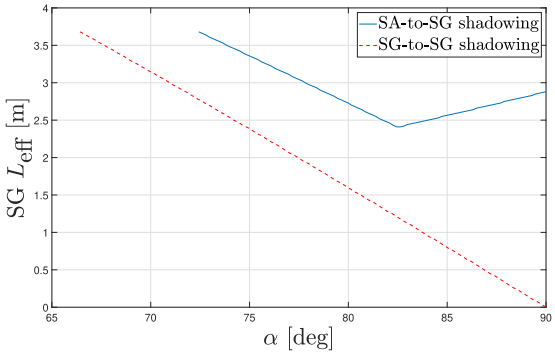

Fig. 25. Variation of SG shadowing size $L_{\text{eff}}(\alpha)$ (SA-to-SG and SG-to-SG cases.

ACKNOWLEDGMENT

The authors would like to acknowledge the support provided by Dr. Pilar Mingorance and Dr. Thomas Bader from the European Space Agency on the SA power subsystem analysis. The authors would like to thank Dr. Miguel Á. Vazquez from the Centre Tecnològic de Telecomunicacions de Catalunya (CTTC) for inspiring the analysis of the phased-array narrowband/wideband model.

REFERENCES

[1] M. Hossein, J. Choi, S.-H. Chang, and J. Lee, "Review of 5G NTN standards development and technical challenges for satellite integration with the 5G network," *IEEE Aerosp. Electron. Syst. Mag.*, vol. 36, no. 8, pp. 22–31, Aug. 2021.

[2] R. D. Gaudenzi, M. Luise, and L. Sanguinetti, "The open challenge of integrating satellites into (beyond-) 5G cellular networks," *IEEE Netw.*, vol. 36, no. 2, pp. 168–174, Mar./Apr. 2022.

[3] G. Bacci, R. D. Gaudenzi, M. Luise, L. Sanguinetti, and E. Sebastiani, "Formation-of-arrays (FoA) antenna technology for high-throughput mobile nonterrestrial networks," *IEEE Trans. Aerosp. Electron. Syst.*, vol. 59, no. 5, pp. 4919–4935, Oct. 2023.

[4] "Low earth orbit mechanical deployable structure," Patent International Publication Number WO2020/232 386 A1, 2020.

[5] A. Guidotti et al., "Architectures and key technical challenges for 5G systems incorporating satellites," *IEEE Trans. Veh. Technol.*, vol. 68, no. 3, pp. 2624–2639, Mar. 2019.

[6] "Study on new radio (NR) to support non terrestrial networks (Rel. 15, v15.1.0)," 3GPP Std. Tech. Rep. 38.811 v15.4.0, Oct. 2020.

[7] R. J. Mailloux, *Phased Array Antenna Handbook*, 3rd ed., Norwood, MA, USA: Artech House, 2018.

[8] A. Caon, M. Doerre, J. Haines, and S. Landstroem, "The GOCE electrical power system," in *Proc. Intersociety Energy Convers. Eng. Conf.*, 2002, pp. 87–92.
[9] M. Amann, M. Gross, and H. Thamm, "The GRACE FOLLOW-ON quiet electrical power system," in *Proc. Eur. Space Power Conf.*, 2016.
[10] G. Bonhours et al., "A new generation of electrical power supply for telecom satellites," in *Proc. Eur. Space Power Conf.*, 2014.
[11] C. Zimmermann, A. Bals, A. Übner, F. Schlerka, and A. Schindler, "Development of a new high-power solar array for telecommunication satellites," in *Proc. Eur. Space Power Conf.*, 2016.
[12] B. Steinberg, *Principles of Aperture and Array System Design - Including Random and Adaptive Arrays*. Hoboken, NJ: Wiley, 1978.
[13] Y. Lo, "A mathematical theory of antenna arrays with randomly spaced elements," *IEEE Trans. Antennas Propag.*, vol. 12, no. 3, pp. 257–268, May 1964.
[14] M. Skolnik, J. Sherman, and F. Ogg, "Statistically designed density tapered arrays," *IEEE Trans. Antennas Propag.*, vol. 12, no. 4, pp. 408–417, Jul. 1964.
[15] M. Viganò, G. Toso, G. Caille, C. Mangenot, and I. Lager, "Sunflower array antenna with adjustable density taper," *Int. J. Antennas Propag.*, vol. 2009, no. 1, pp. 1–10, 2009.
[16] G. D. Mauro, M. Lawn, and R. Bevilacqua, "Survey on guidance navigation and control requirements for spacecraft formation-flying missions," *AIAA J. Guid., Control, Dyn.*, vol. 41, no. 3, pp. 581–602, 2018.
[17] G.-P. Liu and S. Zhang, "A survey on formation control of small satellites," *Proc. IEEE*, vol. 106, no. 3, pp. 440–457, Mar. 2018.
[18] J. A. Nanzer, S. R. Mghabghab, S. M. Ellison, and A. Schlegel, "Distributed phased arrays: Challenges and recent advances," *IEEE Trans. Microw. Theory Techn.*, vol. 69, no. 11, pp. 4893–4907, Nov. 2021.
[19] L. Pan, T. Jiang, L. Zhou, H. Xu, and W. Chen, "A research on high-precision time-synchronization and ranging system between satellites," in *Proc. Int. Conf. Microw. Millimeter Wave Technol.*, 2008, pp. 926–929.
[20] X. Jiuling, Z. Chaojie, W. Chunhui, and J. Xiaojun, "Approach to inter-satellite time synchronization for micro-satellite cluster," *J. Syst. Eng. Electron.*, vol. 29, no. 4, pp. 805–815, 2018.
[21] J. A. Nanzer, R. L. Schmid, T. M. Comberiate, and J. E. Hodkin, "Open-loop coherent distributed arrays," *IEEE Trans. Microw. Theory Techn.*, vol. 65, no. 5, pp. 1662–1672, May 2017.
[22] R. L. Schmid, T. M. Comberiate, J. E. Hodkin, and J. A. Nanzer, "One-way wireless clock transfer for coherent distributed arrays," in *Proc. IEEE Radio Wireless Symp.*, 2017, pp. 19–21.
[23] S. Mghabghab, H. Ouassal, and J. A. Nanzer, "Wireless frequency synchronization for coherent distributed antenna arrays," in *Proc. IEEE Int. Symp. Antennas Propag. USNC-URSI Radio Sci. Meeting*, 2019, pp. 1575–1576.
[24] P. Angeletti and R. D. Gaudenzi, "A pragmatic approach to massive MIMO for broadband telecommunication satellites," *IEEE Access*, vol. 8, pp. 132212–132236, 2020.
[25] P. Angeletti and R. D. Gaudenzi, "Heuristic radio resource management for massive MIMO in satellite broadband communication networks," *IEEE Access*, vol. 9, pp. 147164–147190, 2021.
[26] P. Angeletti and R. D. Gaudenzi, "Optimizing massive MIMO design for non uniform traffic in broadband telecommunication satellites networks," *IEEE Access*, vol. 11, pp. 113493–113513, 2023.
[27] J. Frank and T. Cheston, "Array Antennas," in *Radar Handbook*, M. Skolnik, Ed., New York, NY, USA: McGraw-Hill, 1970, ch. 11.
[28] J. Frank, "Bandwidth criteria for phased arrays," in *Phased Array Antennas*, A. Oliner and G. Knittel, Eds., Dedham, MA, USA: Artech House, 1972, pp. 243–253.
[29] G. Knittel, "Relation of radar range resolution and signal-to-noise ratio to phased-array bandwidth," *IEEE Trans. Antennas Propag.*, vol. 22, no. 3, pp. 418–426, May 1974.
[30] M. R. Patel and R. K. Arora, "Array dispersion effects on matched filter output for a linear FM signal," *IEEE Trans. Aerosp. Electron. Syst.*, vol. AES-14, no. 4, pp. 700–703, Jul. 1978.
[31] W. W. Shrader, "Universal design curves for effects of dispersion in phased array radars," in *Proc. Eur. Microw. Conf.*, 1985, pp. 566–571.
[32] R. L. Haupt, "Factors that define the bandwidth of a phased array antenna," in *Proc. IEEE Int. Symp. Phased Array System Technol.*, 2019, pp. 1–4.
[33] R. Tang, "Survey of time-delay beam steering techniques," in *Phased Array Antennas*, A. Oliner and G. Knittel, Eds., Dedham, MA, USA: Artech House, 1972, pp. 254–260.
[34] R. Rotman, M. Tur, and L. Yaron, "True time delay in phased arrays," *Proc. IEEE*, vol. 104, no. 3, pp. 504–518, Mar. 2016.
[35] D. B. Ward, "Theory and design of broadband sensor arrays with frequency invariant far-field beam patterns," *J. Acoustical Soc. Amer.*, vol. 97, pp. 1023–1034, 1995.
[36] A. Goldsmith, *Wireless Communications*. Cambridge, U.K.: Cambridge Univ. Press, 2005.
[37] T. Laakso, V. Vlaimaki, M. Karjalainen, and U. Laine, "Splitting the unit delay [FIR/all pass filters design]," *IEEE Signal Process. Mag.*, vol. 13, no. 1, pp. 30–60, Jan. 1996.
[38] Y. Cailloce, G. Caille, I. Albert, and J. Lopez, "A Ka-band direct radiating array providing multiple beams for a satellite multimedia mission," in *Proc. IEEE Int. Conf. Phased Array Syst. Technol.*, 2000, pp. 403–406.
[39] G. Toso, C. Mangenot, and A. Roederer, "Sparse and thinned arrays for multiple beam satellite applications," in *Proc. ESA Antenna Workshop Mult. Beams Reconfigurable Antennas*, 2007, pp. 1–4.
[40] P. Angeletti and G. Toso, "Aperiodic arrays for space applications: A combined amplitude/density synthesis approach," in *Proc. Eur. Conf. Antennas Propag.*, 2009, pp. 2026–2030.
[41] G. Toso, P. Angeletti, and C. Mangenot, "A comparison of density and amplitude tapering for transmit active arrays," in *Proc. Eur. Conf. Antennas Propag.*, 2009, pp. 840–843.
[42] P. Angeletti and G. Toso, "Optimal amplitude–density synthesis of linear aperiodic arrays," *IEEE Trans. Antennas Propag.*, vol. 71, no. 6, pp. 4903–4918, Jun. 2023.
[43] R. Haupt, "Splitting the unit delay—Tools for fractional delay filter design," *IEEE Trans. Antennas Propag.*, vol. 41, no. 2, pp. 993–999, 1993.
[44] M. Viganò, G. Toso, S. Selleri, C. Mangenot, P. Angeletti, and G. Pelosi, "Direct radiating thinned arrays for a multibeam coverage," in *Proc. ESA Antenna Workshop Mult. Beams Reconfigurable Antennas*, 2007.
[45] M. Viganò, G. Toso, S. Selleri, C. Mangenot, P. Angeletti, and G. Pelosi, "GA optimized thinned hexagonal arrays for satellite applications," in *Proc. IEEE Antennas Propag. Soc. Int. Symp.*, 2007, pp. 3165–3168.
[46] I. Bekey, "Formation flying picosat swarms for forming extremely large apertures," in *Proc. Workshop Innov. System Concepts*, 2006, pp. 59–66.
[47] G. Maral, M. Bousquet, and Z. Sun, *Satellite Communication Systems*. New York, NY: Wiley, 2020.
[48] R. M. Sumanth, "Computation of eclipse time for low-earth orbiting small satellites," *Int. J. Aviation, Aeronaut., Aerosp.*, vol. 6, no. 5, pp. 1–13, 2019.
[49] A. Fernández, G. D'Accolti, B. Buergler, and B. García, "PEPS. A tool for power system simulation," in *Proc. Eur. Space Power Conf.*, 2014.
[50] D. Alexandrescu, M. Glorieux, V. Correas, I. Nofal, and D. Levacq, "Applicability of FinFET technologies for space applications," in *Proc. Int. W. Analogue Mixed-Signal Integr. Circuits Space Appl.*, 2021.

Giacomo Bacci (Senior Member, IEEE) received the Ph.D. degree in information engineering from the University of Pisa, Pisa, Italy, in 2008.

From 2006 to 2007, he was a Visiting Student Research Collaborator with Princeton University, Princeton, NJ, USA. From 2008 to 2014, he was a Postdoctoral Research Fellow with the University of Pisa. From 2008 to 2012, he was also a Software Engineer with Wiser Srl, Livorno, Italy, and from 2012 to 2014, he was a Visiting Postdoctoral Research Associate with Princeton University. From 2015 to 2021, he was a Product Manager for interactive satellite broadband communications with MBI Srl, Pisa. Since 2022, he joined the University of Pisa as a tenure-track Assistant Professor.

Dr. Bacci was the recipient of the FP7 Marie Curie International Outgoing Fellowships for career development (IOF) 2011 GRAND-CRU, the Best Paper Award from the IEEE Wireless Communications and Networking Conference (WCNC) in 2013, the Best Student Paper Award from the International Waveform Diversity and Design Conference (WDD) in 2007, the Best Session Paper at the ESA Workshop on EGNOS Performance and Applications in 2005, and the 2014 URSI Young Scientist Award. He is currently an Associate Editor for *IEEE Communications Letters* and *EURASIP Journal on Advances in Signal Processing*, and a Senior Member of the International Union of Radio Science.

Riccardo De Gaudenzi (Fellow, IEEE) received the Doctor Engineer degree (cum laude) in electronic engineering from the University of Pisa, Pisa, Italy in 1985, the Ph.D. degree in code division multiple access for satellite personal communication systems from the Technical University of Delft, Delft, The Netherlands, in 1999, and the master's degree ad honorem in communication engineering from the University of Parma, Parma, Italy, in 2021.

He has authored or coauthored more than 140 scientific papers and owns more than 30 patents. He actively contributed to the development and the demonstration of the ETSI S-UMTS Family A, S-MIM, DVB-S2, DVB-S2X, DVB-RCS2 and DVB-SH standards. From 1986 to 1988, he was with the European Space Agency (ESA), Stations and Communications Engineering Department, Darmstadt, Germany, where he was involved in satellite Telemetry, Tracking and Control (TT&C) ground systems design and testing. In 1988, he joined ESA's Research and Technology Centre (ESTEC), Noordwijk, The Netherlands, where he has been covering several technical and managerial positions inside the Directorate of Technology, Engineering and Quality. He is currently the Head of the Department of Electrical Engineering, ESA. He has led a large number of R&D activities for TT&C, Telecom and Navigation applications. In 1996, he spent one year with Qualcomm Inc., San Diego, USA, in the Globalstar LEO project system group under an ESA fellowship. His current research interests include efficient digital modulation and multiple access techniques for fixed and mobile satellite services, synchronization topics, adaptive interference mitigation techniques, and communication systems simulation techniques.

Dr. De Gaudenzi was a corecipient of the 2003 and 2008 Jack Neubauer Memorial Award Best Paper from the IEEE Vehicular Technology Society, and the recipient of the AIAA 2022 Aerospace Communications Award. From 2001 to 2005, he was Associate Editor for CDMA and Synchronization for IEEE TRANSACTIONS ON COMMUNICATIONS and an Associate Editor for *Journal of Communications and Networks*.

Marco Luise (Fellow, IEEE) received the M.Sc. (laurea) and Ph.D. degrees in electronic engineering from the University of Pisa, Pisa, Italy, in 1984 and 1989, respectively.

He is a Professor of telecommunications with the University of Pisa, and with the University of Florence, Florence, Italy. He was a Research Fellow with the European Space Agency. He has chaired a number of scientific conferences, including IEEE ICASSP 2014 in Florence, Italy, and IEEE ICC 2023 in Rome, Italy. He has authored or coauthored more than 300 publications. His main research interests include the broad area of wireless/satellite communications and positioning.

Dr. Luise was the Editor of IEEE TRANSACTIONS ON COMMUNICATIONS. He is a Division Editor for *Journal of Communications and Networks*, and was the coordinator of the European Network of Excellence in Wireless Communications NEWCOM#.

Elena Sebastiani received the B.E. and the M.E. degrees in aerospace engineering in 2017 and 2020, respectively, from the University of Pisa, Pisa, Italy, where she is currently working toward the Ph.D. degree in information engineering.

Since 2021, she has been with Wiser Srl, Livorno, Italy. Her research interests include satellite payload, antenna design for space applications, and satellite constellations.

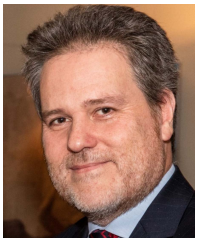

Piero Angeletti (Senior Member, IEEE) received the Laurea degree in electronics engineering (summa cum laude) from the University of Ancona, Ancona, Italy, in 1996, and the Ph.D. degree in electromagnetism from the University of Rome "La Sapienza," Rome, Italy, in 2010.

He is heading the Radio Frequency Payloads and Technology Division of the ESA Directorate of Technology, Engineering and Quality (TEC), which is responsible for RF payloads, instruments, and relevant technologies. In particular, he oversees ESA R&D activities related to flexible satellite payloads, RF front-ends, and onboard digital processors. He has more than 20 years experience in RF Systems engineering and technical management encompasses conceptual/architectural design, tradeoffs, detailed design, production, integration and testing of satellite payloads and active antenna systems for commercial/military telecommunications and navigation (spanning all the operating bands and set of applications) as well as for multifunction RADARs and electronic counter measure systems. He has authored or coauthored more than 300 technical reports, book chapters, and papers published in peer reviewed professional journals and international conferences' proceedings. He holds several patents related to satellite payload and antenna technology.

Dr. Angeletti is currently a Member of the technical staff of the European Space Research and Technology Center (ESTEC), European Space Agency, Noordwijk, The Netherlands. Together with Giovanni Toso, he is instructor of the course on "Multibeam Antennas and Beamforming Networks" which, since 2012, has been offered at main IEEE and European microwaves, wireless and antenna conferences (IEEE APS, IEEE IMS, EuMW, EuCAP, IEEE ICWITS, ESA Internal University, etc.). In 2022, he was the recipient of S. A. Schelkunoff award by the IEEE Antennas and Propagation Society for the best IEEE TAP paper published in 2021, Angeletti and Lizarraga, "Traffic Balancing Multibeam Antennas for Communication Satellites."

José Ramón González was born in Madrid, Spain, in 1976. He received the M.Sc. degree in physics from Universidad Complutense of Madrid (UCM), Madrid, Spain, in 2002, and the Ph.D. degree (cum laude) in photovoltaic energy from the Polytechnic University of Madrid (UPM), Madrid, Spain, in 2008.

In 2013, he joined the ESA's Research and Technology Centre (ESTEC), Noordwijk, The Netherlands, where he holds a position as Solar Cell and Solar Generator Engineer with the Solar Generators Section, Electrical Department. His main research interests include manufacturing and characterization of III-V based multijunction solar cells and solar arrays, including inorbit performance prediction and verification.

Open Access provided by 'Università di Pisa' within the CRUI CARE Agreement